agriculture

MDPI

Article

Multivariate Structural Vibration Coupling Response of the Self-Propelled Straw Pickup Baler Under Time-Varying Loads

Bangzhui Wang [1], Kexin Que [1], Zhong Tang [1,2,*], Meiyan Sun [3], Yi Lian [3] and Haoyang Wang [1]

[1] School of Agricultural Engineering, Jiangsu University, Zhenjiang 212013, China; 2222316058@stmail.ujs.edu.cn (B.W.); 3222502002@stmail.ujs.edu.cn (K.Q.); 18262885309@163.com (H.W.)
[2] Key Laboratory of Modern Agricultural Equipment and Technology, Ministry of Education, Jiangsu University, Zhenjiang 212013, China
[3] College of Transportation Engineering, Jiangsu Shipping College, Nantong 226010, China; smy201314@jssc.edu.cn (M.S.); lianyi@jssc.edu.cn (Y.L.)
* Correspondence: zht@ujs.edu.cn

Abstract: The self-propelled straw pickup baler in agricultural work is responsible for collecting and compressing straw to facilitate transportation and storage, while reducing waste and environmental pollution. Like other agricultural equipment, the straw pickup baler is a complex mechanical system. During operation, its excitation characteristics under multi-source stimuli and the coupling characteristics of various components are not yet clear. This paper analyzed the excitation mechanics property of each component of the self-propelled straw pickup baler and established balance equations. Based on the balance equations, the coupling characteristics of the structures were studied. Through experiments collecting excitation signals from multiple devices under different operating conditions, the vibration excitation signals of each component were obtained. The experiments revealed that the excitation and coupling signals in the Z direction are particularly evident. Based on experiments, the effective Z-direction vibration signal value on the left front of the chassis exceeds 7 $m{\cdot}s^2$, while on the right front it increases from 1.995 $m{\cdot}s^2$ to 7.287 $m{\cdot}s^2$, indicating the most intense vibration direction. It was also found that, at the driver's cab, the effective Z-direction vibration signal values at two response points, 11 and 12, both exceed 7 $m{\cdot}s^2$. The data indicate significant vibrations occur in both the longitudinal and vertical directions. Using the Signal Analyzer module in MATLAB for signal processing, it was found that the prominent filtered signals consist of combustion excitation harmonics and continuous low-frequency vibrations from the compression mechanism. The periodic reciprocating compression motion of the crank-slider mechanism causes sustained impacts on the frame, leading to periodic changes in the vibration amplitude of the chassis. Thus, the vibration reduction of the compression mechanism's periodic motion is key to reducing the overall vibration of the machine.

Keywords: signal analysis; incentive coupling; fault analysis; straw pickup baler; agricultural equipment

Citation: Wang, B.; Que, K.; Tang, Z.; Sun, M.; Lian, Y.; Wang, H. Multivariate Structural Vibration Coupling Response of the Self-Propelled Straw Pickup Baler Under Time-Varying Loads. *Agriculture* **2024**, *14*, 1960. https://doi.org/10.3390/agriculture14111960

Academic Editor: John M. Fielke

Received: 18 October 2024
Revised: 29 October 2024
Accepted: 30 October 2024
Published: 1 November 2024

1. Introduction

The self-propelled straw pickup baler, as a commonly used agricultural equipment, is a complex multi-component machine with several intricate working devices [1–3]. Due to the complicated working environment, fatigue failure of agricultural equipment is inevitable, and machine failure frequently arises from the coupling and superposition of self-excitation [4,5]. Additionally, during operation, agricultural machines inevitably come into contact with crops, which can impose impacts and loads on the device structures, thereby affecting their performance [6,7]. Different types and working conditions will lead to varying working intensities and excitations, resulting in different failure modes for the machine's components. Understanding the excitation characteristics of these components and their impact on the machine can improve the working conditions and lifespan of

agricultural equipment [8–10]. The motion modes of structures and the connection methods between working devices are closely related to the characteristics of vibration signals. These signals can not only reflect the normal operational information of each device but also indicate changes in the internal structural performance, which can affect the machine's working efficiency [11–13]. The coupling of internal and external excitations can lead to more intense vibrations and internal excitations, exacerbating fatigue and failure of the device structures, ultimately impacting the performance and lifespan of the combined equipment [14,15]. Furthermore, the coupling of excitations can pose safety risks and generate significant noise, affecting the physical and mental health of operators. Therefore, studying the vibration characteristics of machines can provide a theoretical basis for optimizing mechanical structures and reducing vibrations in agricultural equipment [16–19]. In recent years, as agricultural equipment has evolved towards larger, faster, more efficient, and smarter designs, there is an urgent need to research the failure characteristics and identification methods of structural signals in agricultural machinery to address noise reduction and structural optimization [20,21].

Currently, many scholars study the vibration characteristics and mechanical features of individual devices by disassembling the overall machine into separate components [22–24]. Some researchers have also focused on optimizing device structures to reduce loads and excitations, thereby extending the lifespan of the devices [25–27]. However, with the continuous improvement of dynamic models, the assessment of machine structural failures can also be studied based on actual loads and the dynamic characteristics of the overall structure [28,29]. By measuring the vibration signals of various devices in agricultural equipment, response signals can be obtained, and the fast Fourier transform method can be employed to analyze the frequency domain characteristics of vibrations and noise, thus studying the operational and failure states of the devices [30–32]. Finite element models of failure structures can be established based on the loads and stress characteristics experienced by the devices, allowing for research on the excitations and fatigue life of the structural components [33–35]. Additionally, by constructing excitation load models for failure models based on external machine excitations, failure tests can be conducted to study the failure characteristics of the devices [36,37]. The vibration signal characteristics of the devices can reflect their structural integrity and stability. By analyzing the vibration signals, it is possible to assess the failure of the devices, reducing the time and labor costs associated with failure assessments [38–40]. Combining statistical energy methods and power spectral characteristics can help in the study of the operational feature models of the devices, which can reflect the fluctuations in signal energy under coupled excitation states and reveal the changing laws of excitation characteristics affecting the structures [41–43]. Through research on the excitation characteristics of all devices in the machine, the stress characteristics can be optimized, and multi-scale predictive models of structural vibrations can be constructed. These models can reveal the damage characteristics of the devices, facilitating the assessment and prediction of failures and fatigue [44–47]. Structures such as engines and frames are common optimization points for reducing vibrations in agricultural equipment in many studies [48–50]. Although the external excitation sources for agricultural equipment stem from the working environment, the excitations differ among various types of equipment, and the main excitation characteristics within the devices also vary [51–54]. While simulation and vibration characteristic research methods have been extensively studied in other agricultural equipment, there is relatively little research on measuring the vibration signals of self-propelled straw pickup balers, and analyses of their excitation and coupling characteristics are limited. This article focuses on the self-propelled straw pickup baler as the research subject, describing excitation experiments conducted under various working conditions through the establishment of excitation mechanics analysis and balance equations for each device. The study investigated the vibration signal characteristics under different operational states to explore the excitation and coupling characteristics of the self-propelled straw pickup baler. The experiments revealed that the excitation and coupling signals of the baler's structures are particularly pronounced in the

Z direction, with significant vibrations observed in both longitudinal and vertical directions. Signal analysis using MATLAB's Signal Analyzer module indicated that optimizing the damping of the periodic motion of the compression mechanism is a key factor in reducing overall machine vibrations, providing theoretical references for the structural and vibration reduction optimization of the self-propelled straw pickup baler.

2. Materials and Methods

2.1. The Overall Structure of the Self-Propelled Pickup Baler

The self-propelled straw pickup baler can perform integrated operations such as picking up scattered straw in the field, orderly conveying, compressing, and baling. The overall structure, as shown in Figure 1, mainly consists of a diesel engine, driver's cab, tracked chassis, pickup header, straw drum, conveying fork, and compression device. Based on the analysis of the straw pickup and baling process and operational requirements, the frontmost part of the machine is the pickup header, which collects discarded straw from the field. It is connected to the baler frame via a conveying chute, forming a longitudinal "T" configuration. The baler frame is positioned above the chassis, with the bale output end at the rear, located on one side of the fodder box. The outlet is inclined downward to facilitate the rearward movement of formed bales. The fodder box is directly behind the driver's cab, and its interior serves as the manual bale stacking area.

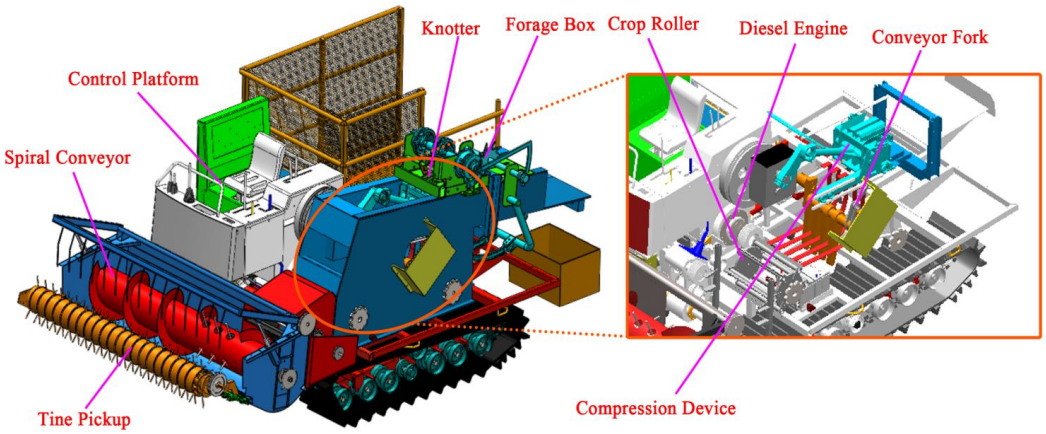

Figure 1. The 3D model structure of the pickup baler.

2.2. The Working Principle of a Pickup Baler

The operational principle and harvesting process of a self-propelled straw pickup baler are illustrated in Figure 2. Before starting field operations, the operator adjusts the header to the appropriate height. During harvesting, the tine pickup at the front of the header first contacts the straw in the field, directing it to the spiral conveyor. The spiral conveyor rotates and transports the straw into the conveyor trough, which then moves it to the pickup drum. The drum feeds the straw beneath the conveyor fork, continuously delivering it to the compression unit's intake. The crank of the compression mechanism rotates at a constant speed, driving the piston to compress the straw repeatedly. As the machine advances, the straw slowly accumulates until it is tied into square bales by the knotter. These bales are then stacked manually in the stacking box. Once a sufficient number of bales are collected, the filled bale frame is lifted by a hydraulic cylinder from below to unload the bales, completing the mechanized process of straw pickup and baling.

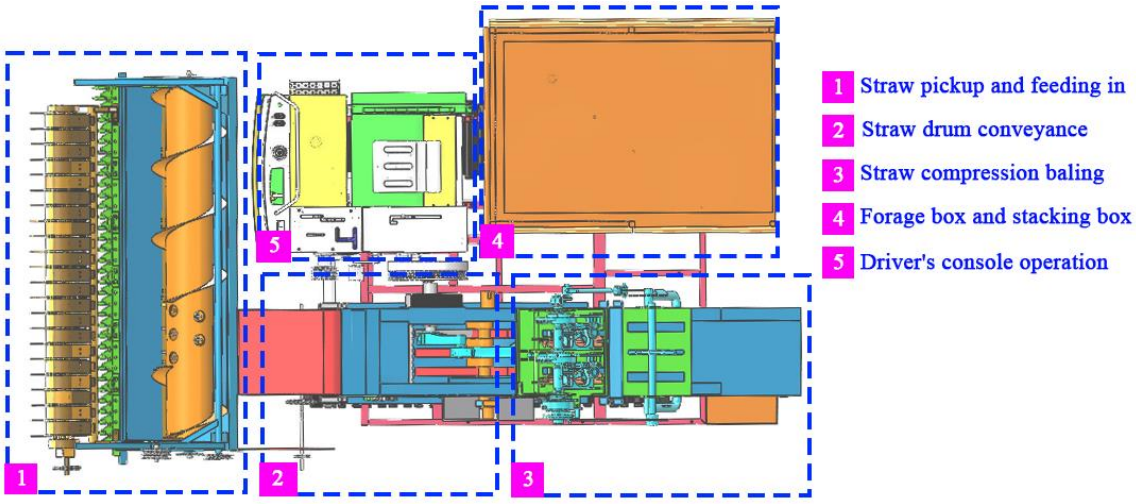

Figure 2. The operation principle and harvesting process of the machine.

A flowchart of the field operations for a self-propelled pickup baler is shown in Figure 3. The machine collects and bales the straw in the field. Then, workers stack the bales from the forage box. The formed bales are unloaded at the field edge, and finally, a truck transports them for subsequent storage and use.

(**a**) (**b**)

Figure 3. Straw harvesting process of the pickup baler. (**a**) Manual bale stacking; (**b**) bale unloading at the field edge.

The frame of the self-propelled pickup baler includes the baler frame and the chassis frame, primarily constructed from welded square steel. The baler frame serves as the mounting base for components like the front and rear grass rakes, conveyor forks, and compression devices, supporting their respective loads. The chassis frame connects to the tracked wheel system to provide support for the entire machine. During field operations, the machine can be analyzed as a multi-degree-of-freedom linear elastic vibration system. The frame experiences vibrations and deformations due to the combined excitation forces from multiple vibration sources, field terrain, and the transmission system. From the above analysis, it is evident that the vibration and coupling of each device have a significant impact on the overall vibration of the machine.

2.3. Theoretical Analysis of the Excitation Characteristics of the Main Vibration Sources in the Pickup Baler

The self-propelled pickup baler has a complex structure with multiple excitation sources. Each key component has different installation and movement methods, leading to constantly changing vibration states. The main excitation sources include the diesel engine, pickup feeding device, grass conveying device, and straw compression device. The vibration of the four-cylinder diesel engine is mainly due to combustion excitation and

inertial force excitation, caused by the periodic variable force of the crankshaft's reciprocating rotational movement. The pickup device's vibration is primarily due to alternating excitation forces generated by the variable mass rotational movement of the tine-type pickup. The grass conveying device's vibration arises mainly from the rotational movement of the grass drum and conveying forks. The straw compression device's vibration is mainly due to the periodic impact from the reciprocating rotational movement of the crank-slider mechanism. Additionally, the transmission system and random vibrations from the field surface also contribute to the vibrations of the self-propelled pickup baler, making the machine's vibration state a result of the combined effect of multiple excitation sources.

2.3.1. Mechanical Analysis of Components and Establishment of Their Equilibrium Equations

The analysis of the mechanical relationships of key moving components to establish corresponding equilibrium equations can provide reference for the subsequent analysis of the theoretical vibration excitation characteristics of each device. To facilitate further mechanical analysis, a Cartesian coordinate system is established based on the body of the pickup baler. The machine's forward direction is defined as the positive X direction, the driver's left side as the positive Y direction, and upward perpendicular to the ground as the positive Z direction.

The simplified model of the pickup header device is shown in Figure 4, illustrating the mechanical equilibrium relationship between the header and the conveyor trough.

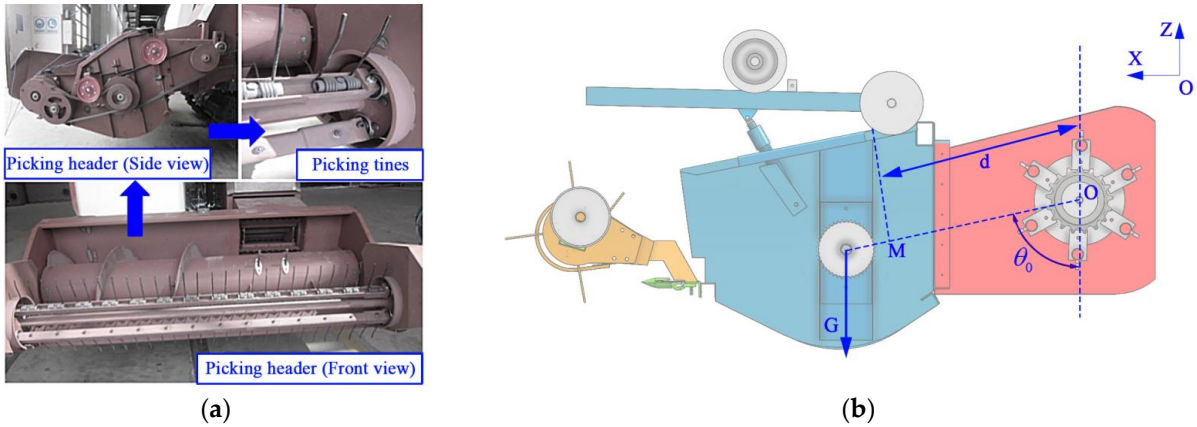

(**a**) (**b**)

Figure 4. Schematic of the pickup header device. (**a**) Actual image of pickup header; (**b**) force diagram of the header and conveyor trough positions.

The point M represents the centroid of the pickup header device, which can be considered as a cantilever structure swinging up and down around the drive shaft of the grass-tine drum within the conveyor trough. The suspension point of the grass-tine drum's drive shaft is marked as point O. When the entire structure undergoes small oscillations in the XOZ plane, the angle θ between the conveyor trough and the vertical direction is chosen as the generalized coordinate, and J_0 represents the rotational inertia of the entire pickup header device. Therefore, when the angular displacement of the device is θ_0, the restoring torque due to the structure's weight is $Gdsin\theta_0$. Therefore, the equation of motion of the system is:

$$J_0\ddot{\theta} + Gdsin\theta_0 = 0 \quad (1)$$

Considering the small oscillations of the pickup header device during operation, the $sin\theta_0$ can be approximated as θ_0 to obtain:

$$J_0\ddot{\theta} + Gd\theta_0 = 0 \quad (2)$$

Since the connection between the conveyor trough and the main frame is rigid, the system's motion equation can be simplified to a second-order homogeneous linear differential equation without damping. The analytical expression for the oscillation amplitude over time and the expression for the natural angular frequency are as follows:

$$\theta_0 = C_1 + C_2 t - \frac{G\dot{\theta}_0 t^2}{2J_0} \tag{3}$$

$$\omega_n = \left(\frac{Gd}{J_0}\right)^{\frac{1}{2}} \tag{4}$$

In the equation, C_1 and C_2 are the constant coefficients in the analytical expression, determined by the system's motion state. ω_n is the natural angular frequency of the overall oscillation of the pickup header device, which is related to the system's structural parameters and mass, and can thus be considered constant.

The front and rear grass rakes are located within the conveyor trough and the baler frame, respectively, and are used to transport the straw picked up by the header backwards into the feed chamber. The input power is provided by a sprocket at point A, and both ends are supported by bearing seats. Mechanical analysis can be conducted axially and radially. The actual and mechanical analysis schematic diagrams are shown in Figure 5.

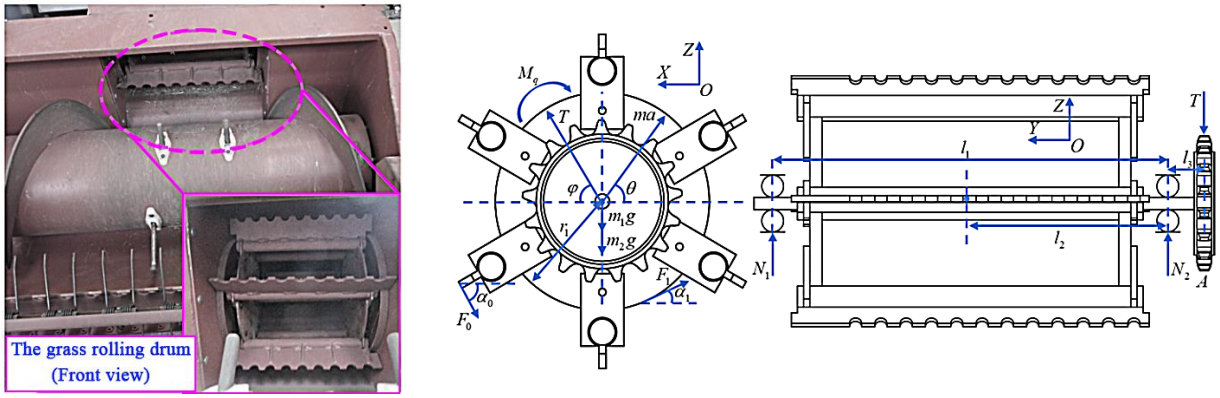

Figure 5. Mechanical analysis diagram of crop roller. (**a**) The front view of crop roller; (**b**) force model of crop roller.

The driving force at the drum shaft end can be equivalent to a torque M_q and a tension T at point A. The drum's own weight is $m_1 g$, with a radius of r_1. The weight of the straw transported by the drum is $m_2 g$. The length of the grass rake plate is l_0. The contact force of the straw on the grass rake plate is simplified as an equivalent force F_0, perpendicular to the plate, with an angle to the horizontal. The rotational resistance of the straw on the drum is F_1, also with an angle to the horizontal. The rotational inertia force of the drum is ma, with an angle to the horizontal. From the axial force analysis model, it can be observed that the distance between the bearing seats at both ends is l_1, and the distance from the drum's center of gravity to the input end bearing seat is l_2. The bearings at both ends provide reaction forces N_1 and N_2. Thus, the mechanical equilibrium equations for the crop roller can be established as follows:

$$\begin{cases} \sum F_x = 0 = N_{1x} + N_{2x} + T\cos\phi + ma\cos\theta + F_0\cos\alpha_0 + F_1\cos\alpha_1 \\ \sum F_y = 0 \\ \sum F_z = N_{1z} + N_{2z} + T\sin\phi + ma\sin\theta + F_0\sin\alpha_0 + F_1\sin\alpha_1 - (m_1 + m_2)g \end{cases} \tag{5}$$

From the equation, it can be observed that in an ideal operating state, the axial force on the crop roller can be ignored. However, as a rotating component, the torque caused by the driving force is significant and satisfies the equilibrium relationship shown in the formula:

$$\begin{cases} M_q + (l_0 + r_1)F_0 + rF_1 + (l_3 + l_2)T\sin\phi + (l_1 - l_2)N_{1z} + l_2N_{2z} = 0 \\ (l_1 - l_2)N_{1x} + l_2N_{2x} + (l_3 + l_2)T\cos\phi = 0 \end{cases} \tag{6}$$

Next, a static analysis of the compression device is conducted to obtain the motion characteristics of each component during the compression process. The force analysis schematic diagram of the components in the compression mechanism is shown in Figure 6. The downward vertical direction is defined as the positive direction. For the convenience of calculation and analysis, it is assumed that there is no gap movement between each connection point and that friction is zero. The components are treated as rigid bodies, meaning there is no elastic deformation during motion. The output main shaft of the reducer drives the crank to rotate counterclockwise at a constant speed. Driven by the crank, the compression device performs periodic reciprocating compression operations within the XOZ plane, thereby providing sufficient compression power to the straw and grass pieces.

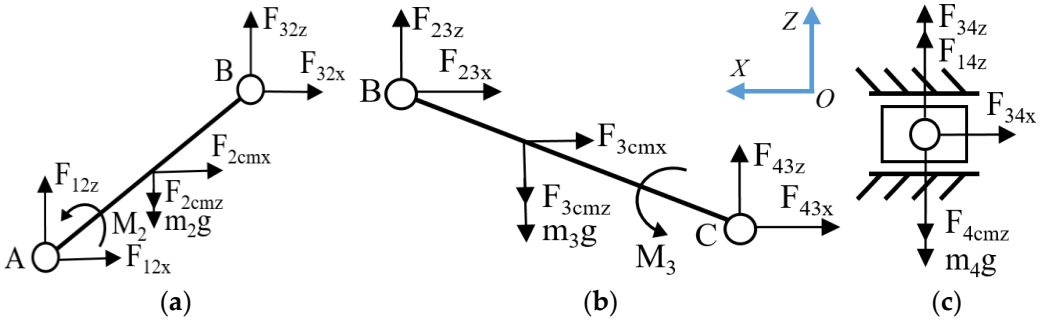

Figure 6. Interaction forces between connected kinematic pairs. (**a**) Force schematic diagram of the crank; (**b**) force schematic diagram of the connecting rod; (**c**) force schematic diagram of the piston.

The excitation generated by the compression device during operation is mainly transmitted to the baler frame through points A and C, which correspond to the connection between the crank's drive shaft and the reducer, and the contact position between the reciprocating compression piston and the sliding rails on both sides, respectively. Therefore, based on the principle of force balance using dynamic and static methods, the interaction force balance relationships between the components of the connected kinematic pairs can be calculated. The balance relationships are represented by Equations (7)–(9):

$$\begin{cases} F_{1x} + F_{2cmx} + F_{32x} = 0 \\ F_{12z} + F_{32z} - F_{2cmz} - m_2g = 0 \\ M_2 + m_2gr_{Acmz} - F_{32z}r_{2x} - F_{32x}r_{2x} = 0 \end{cases} \tag{7}$$

$$\begin{cases} F_{23x} + F_{3cmx} + F_{43x} = 0 \\ F_{43z} + F_{23z} - F_{3cmz} - m_3g = 0 \\ M_3 + F_{43z}l_{Ccmz} + F_{43x}l_{Ccmz} - F_{23z}l_{Bcmz} - F_{23x}l_{Bcmz} = 0 \end{cases} \tag{8}$$

$$\begin{cases} m_4\ddot{a}_x = -Fcos\phi = F_{34x} \\ m_4\ddot{a}_z = Fson\phi + F_{14z} - m_4g = F_{34z} \end{cases} \tag{9}$$

In addition, to obtain the magnitude of the force exerted by the connecting rod on the compression piston, substituting Equation (10) into (11) yields:

$$F = ml\left[\frac{\omega^2 rcos\theta}{\sqrt{l^2 - (r\sin\theta)^2}} + \omega^2 r^2 cos2\theta + \frac{\left(r^2\omega\sin\theta cos\theta\right)^2}{l^2 - (r\sin\theta)^2}\right] \tag{10}$$

$$F_{14z} = m_4 g - F\frac{r}{l}sin\theta \tag{11}$$

From the force balance relationship expressed by Equation (7), it can be seen that the force at the connection point A of the baler frame mainly arises from the inertial force of the crank's center of mass, gravity, and the driving torque. In addition, according to Equation (10), it can be determined that the magnitude of the force F exerted by the connecting rod on the compression piston is solely related to the crank length, connecting rod length, compression piston mass, crank rotational speed, and angular position. Analyzing Equation (9), it is concluded that the excitation of the compression device on the baler frame is primarily divided into the X direction and Z direction. Moreover, due to the motion constraints of the sliding rails, the excitation transmitted in the Z direction will be significantly smaller than that in the X direction.

2.3.2. The Theoretical Analysis of Vibration Excitation Forces of Each Device

By analyzing the mechanical equilibrium relationships of key moving components, it can be observed that the excitation forces transmitted to the frame exhibit different time-varying nonlinear characteristics due to the varying forms of motion and force characteristics of each device. Therefore, during the field operations of the self-propelled straw pickup baler, the excitation forces between various key working components will interact and give rise to complex coupling and resonance phenomena, making it difficult to analyze the excitation forces transmitted to the frame at that time. Thus, by analyzing the individual excitation forces of the key moving components, the corresponding theoretical excitation characteristics of the devices can be obtained.

For the pickup header device, the main moving components are the tine picker and the spiral conveyor. The rotation of the drive shafts of these two components during operation results in torsional vibrations, and the excitation is mainly transmitted through the connection points with the conveying trough. Therefore, disregarding the mass of the drive shafts, let us assume that the initial rotation angles of the drive shafts are denoted as α_0 and ϕ_0, respectively, where ω_1 and ω_2 represent the natural angular frequencies of the two components. The angular displacements of the two components during the rotation time tt are denoted as α_1 and ϕ_1, respectively. Thus, the angular displacements can be expressed as shown in Equation (12):

$$\begin{cases} \alpha_1 = \alpha_0 cos\omega_1 t + \frac{\alpha_0'}{\omega_1'}\sin\omega_1 \\ \phi_1 = \phi_0 cos\omega_2 t + \frac{\phi_0'}{\omega 2}\sin\omega_2 t \end{cases} \tag{12}$$

Therefore, the excitation force of the pickup header device can be calculated based on the angular displacement formula, expressed as Equation (13):

$$F = m_1\phi_0'' + m_2\alpha_0'' \tag{13}$$

At the same time, it can be observed that the theoretical excitation forces of each device on the frame, under stable operating conditions, are composed of superimposed simple harmonic signals of single or multiple frequencies. The reaction force at the connection points is balanced by the system's gravity and inertial forces. Therefore, under the rotational

excitation of the drive shafts of the key moving components of the pickup baler, the corresponding theoretical excitation forces of the devices can be uniformly expressed as:

$$\begin{cases} \omega_k = 2\pi f_k = 2\pi \cdot \frac{n_k}{60} \\ F_k = k_k + \sum_{n=1}^{m} A_n cos(n_k \omega_k t + \theta_n) \end{cases} \quad (14)$$

In the equation, ω_k is the angular velocity of the drive shaft of the moving component, rad/s; f_k is the rotational frequency of the drive shaft, Hz; n is the rotational speed of the drive shaft, r/min; F_k is the theoretical excitation force of the moving component, N; k_k is the constant in the theoretical excitation force, N; and m is the number of different frequency components obtained from the Fourier transform decomposition of the vibration signal. For the diesel engine of the pickup baler, mm is equal to 1; A_n is the amplitude of the nth component in the periodic varying force, N; and θ_n is the initial phase of the nth component in the periodic varying force, rad.

2.4. Analysis of Vibration Response Characteristics in Different Operating States of the Machine Body

During the normal field operation of the entire machine, key moving components such as the pickup header, diesel engine, crop roller, conveying fork, and compression baling device exert support reactions on their supporting structures. Together with the connecting structures, they act as excitation sources, generating nonlinear time-varying excitation forces that are applied to the main frame and transmitted throughout the machine. The intensity of the machine body's vibrations can be reflected by parameters such as the root mean square value of acceleration, peak value, peak-to-peak value, average value, and power spectral density function. This study collected acceleration signal data through vibration signal testing experiments and used time domain and frequency domain analysis methods to explore the excitation characteristics of the key moving components of the machine body and the dynamic response characteristics of the frame under excitation.

To adapt to the operational characteristics of the self-propelled straw picking and baling machine, this experiment employed acceleration sensors with a broad dynamic response range and high sensitivity to collect transient vibration signals. These signals were analyzed through velocity, acceleration, and displacement to assess the motion of the mechanism. The DH5902N dynamic signal acquisition instrument (China, Jangsu) and a three-axis accelerometer were used to receive and record signals, which were then analyzed using dynamic signal analysis software. The IEPE-type sensors used in this experiment came with built-in amplification circuits, and the signal acquisition instrument was equipped with a low-pass anti-aliasing filter. First, a reasonable sampling frequency was set in the signal acquisition instrument according to the sampling theorem. The test procedure employed continuous sampling to obtain vibration signals, ensuring that the sampling frequency was at least twice the analysis frequency. Considering that the main vibration frequencies of the various excitation sources in the baler are all lower than the rotational frequency of the diesel engine (40 Hz), a low-pass anti-aliasing filter frequency (sampling frequency) of 2 kHz was chosen. The parameters of the relevant instruments and equipment used in the experiment are shown in Table 1.

The three-axis accelerometer and dynamic signal acquisition system used in the experiment are shown in Figures 7 and 8, respectively.

During the actual operation of the machine, the operator adjusts the throttle size as needed based on different terrains and working conditions to control the machine's travel speed. Therefore, the engine speed and the speeds of various key moving parts vary under different working conditions. However, to achieve a better harvesting and bundling effect, the engine is often controlled at its rated speed during harvesting, at which point the speeds of various key moving parts can meet the design requirements. The test conditions were divided into indoor and outdoor sites, with the outdoor site mainly used for testing the body vibration during the machine's travel process and the indoor site mainly used for

obtaining the natural vibration characteristics of the machine, as shown in Figure 9. During the testing process, the focus was on analyzing the vibration response characteristics of the machine at various vibration source locations under engine idle and normal operating conditions of the working parts.

Table 1. The experimental instruments and sensor parameters.

Instrument Name	Performance Indicators	Technical Parameters
1A312E Type Accelerometer	Measurement Range (g)	±500
	Frequency Response (kHz)	0.5~10
	Sensitivity (mV/g)	100
	Maximum Cross-Sensitivity (%)	<5
	Resolution (g)	0.001
DH5902N Type Dynamic Signal Acquisition Instrument	Number of Channels	32
	Maximum Sampling Frequency (kHz)	256
	Distortion	<0.5
	Signal Input Method	IEPE

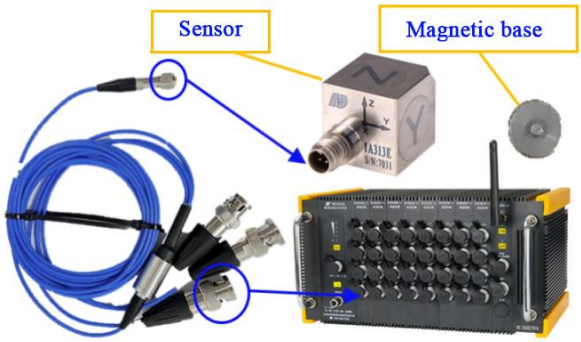

Figure 7. 1A312E type accelerometer.

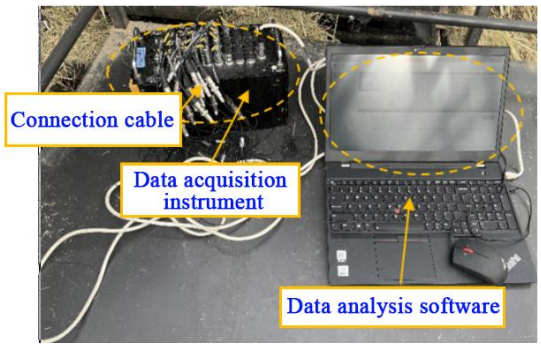

Figure 8. DH5902N type dynamic signal acquisition system.

The vibration of non-road vehicles can be regarded as steady-state random vibration, and studying the effect of idle conditions on the vibration of the whole machine is of great significance. The indoor testing was mainly conducted under static no-load conditions of the whole machine, which can be divided into idle conditions with only the engine running and operational conditions with components running. The outdoor testing was mainly divided into travel conditions with only the engine running and travel conditions with components working, with the forward speed controlled at around 5 km/h. Additionally, to facilitate subsequent data processing and analysis, a Cartesian coordinate system based on the machine's position was established when arranging sensors for measurement after selecting appropriate structural feature points. The forward direction of the operator's seat of the baler was defined as the positive *X*-axis of the sensor, the left side of the seat was the

positive *Y*-axis, and the upward direction perpendicular to the ground was the positive *Z*-axis. The test conditions and the corresponding operating states of the baler are shown in Table 2.

(**a**) (**b**)

Figure 9. Vibration test testing scenarios. (**a**) Engine position measurement point arrangement; (**b**) indoor vibration testing.

Table 2. Test conditions for the self-propelled straw pickup baler.

Test Condition	Operating Status	Test Environment	Forward Speed (km/h)
1	Whole machine static no load (only engine running)	Indoor	0
2	Whole machine static no load (components running)	Indoor	0
3	Whole machine walking (only engine running)	Outdoor	5
4	Whole machine walking (components running)	Outdoor	5

To comprehensively analyze the excitation characteristics of key structural points at different excitation source locations of the whole machine and the vibration response characteristics of the main frame, this experimental study selected a total of 12 measurement points at key structural feature points of the driving shaft of key moving parts and critical positions of the frame. Three-axis sensors were arranged to obtain vibration signals. The excitation signal from the engine was collected by a sensor placed at the transition frame between the output shaft and the flywheel. The distribution locations of each sensor measurement point are shown in Table 3.

Table 3. The distribution locations of measurement points.

Measurement Point	Distribution Location	Measurement Point	Distribution Location
1	Transition frame of engine output shaft	2	Bearing seat of the picker drive shaft
3	Upper end of the front grass rolling drum shaft	4	Upper end of the rear grass rolling drum shaft
5	Bearing seat of the conveying fork drive shaft	6	Bearing seat of the compression mechanism drive shaft
7	Left front of the chassis frame	8	Left rear of the chassis frame
9	Right front of the feed box	10	Right rear of the feed box
11	Seat support of the operator's platform	12	Floor plate of the operator's platform

In order to compare the vibration response characteristics of various excitation sources and the machine body of the self-propelled straw pickup baler under different working conditions, three-axis sensors with magnetic bases were affixed to the bearing seats or mounting beams at the main excitation source locations to obtain time-varying vibration signals. At the same time, structural feature points at the frame and seat support plate positions were selected as response points for the excitation. The installation positions of the sensors and the testing scenarios are shown in Figures 10 and 11.

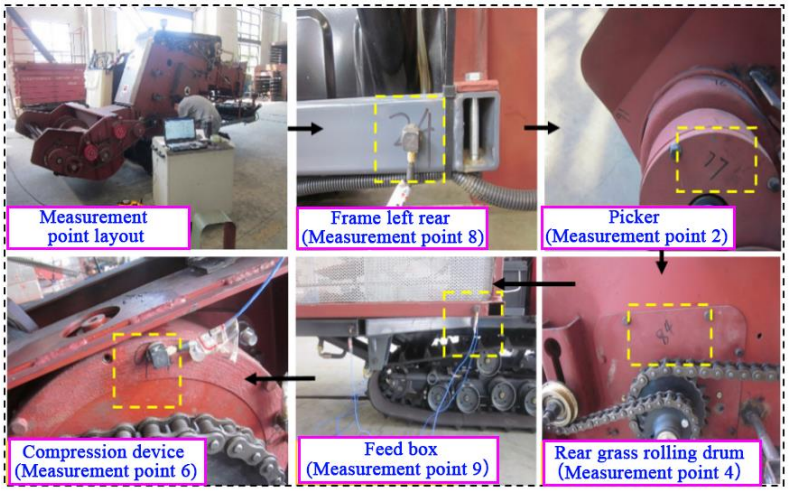

Figure 10. The indoor measurement point arrangement.

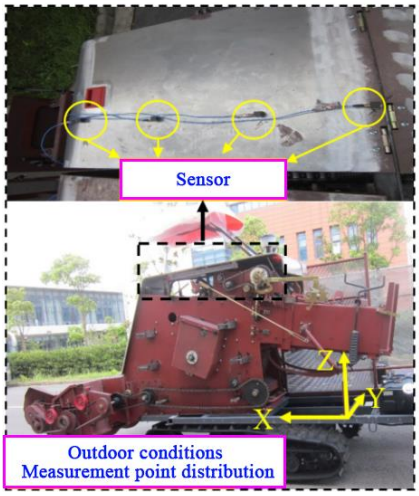

Figure 11. The outdoor measurement point arrangement.

When selecting the operating conditions for the vibration testing of the whole machine, it was primarily considered that the excitation force at the source location of the machine body would change with different working states of the whole machine, and that the vibration response of the frame is also dynamically changing. Therefore, two different conditions were set for analysis: idle excitation at the indoor site (only the engine idling throttle was working) and operation of the whole machine's working components under static no-load conditions. The three-axis sensors data collected from different measurement point locations under each condition would be subjected to time domain analysis and comparison.

2.5. Vibration Signal Acquisition and Processing of the Self-Propelled Straw Pickup Baler

2.5.1. Acquisition and Analysis of Time Domain Vibration Signals

In the processing of vibration signals for engineering machinery, the periodic patterns are generally analyzed to obtain the magnitude of the vibration signal and its variations. The body vibration of the self-propelled straw pickup baler during normal field operations can be considered as steady-state random vibration. For the time domain vibration signals, the root mean square (RMS) value of the acceleration can be calculated to reflect the variation characteristics of the body vibration amplitude. This is also an important parameter for describing the energy changes of steady-state random vibration, and its calculation formula can be expressed as:

$$F_{rms} = \sqrt{\frac{1}{N}\sum_{m=1}^{N} f(m)^2} \tag{15}$$

In the formula, F_{rms} is the root mean square value, N is the number of times the signal is averaged, and $f(m)$ is the acquired vibration signal.

By statistically measuring the maximum peak value of the time domain signal, the limit stress induced by vibration can be obtained, along with the maximum acceleration, velocity, and displacement of the vibration signal. This paper uses the root mean square (RMS) value of acceleration and the peak-to-peak value (the difference between the maximum peak and the maximum trough) to comprehensively describe the intensity of the vibration signal.

In addition, correlation analysis is often used in the processing of time domain signals, mainly including autocorrelation analysis and cross-correlation analysis. Autocorrelation analysis compares the similarity between two signal time series, filtering out random noise from the collected time domain signals and highlighting the regular and periodic signal components. This can be used to detect the periodic vibrations generated during the operation of the self-propelled straw pickup baler, and its calculation formula is:

$$R(\tau) = \lim_{T\to\infty} \frac{1}{T}\int_0^T x(t)x(t+\tau)dt \tag{16}$$

In the formula, $R(\tau)$ is the autocorrelation function (m^2/s^4); τ is the time difference between the signals (s); $x(t)$ is the time domain vibration acceleration signal (m/s^2); and T is the measurement time of the vibration signal (s).

Cross-correlation analysis can compare the similarity between signals at two different moments within the same signal time series, reflecting the general correlation between the two signals. This can be used to analyze the impact of different excitation sources on the vibration response of the machine body, and its calculation formula is:

$$R_{xy}(\tau) = \lim_{T\to\infty} \frac{1}{T}\int_0^T x(t)y(t+\tau)dt \tag{17}$$

In the formula, $R_{xy}(\tau)$ is the cross-correlation function (m^2/s^4); and $y(t)$ is the time domain curve of one of the vibration signals (m/s^2).

2.5.2. Characteristic Analysis of Frequency Domain Signals of the Machine Body

The frequency domain analysis can describe the relationship between frequency and time by calculating the time domain signals and obtaining the frequency components in periodic signal functions. A common method is to use Fourier transform to convert the vibration signal into a sum of trigonometric functions at different frequencies for

signal decomposition. The following transformation formula applies to the collected vibration signals:

$$F(k) = DFT(f(m)) = \sum_{i=0}^{N-1} f(m) e^{-j\frac{2\pi k}{N}m} \tag{18}$$

In the formula, k is the index of the discrete frequency signal, N is the number of sampling points within the analysis interval, and $\frac{2\pi k}{N}$ is the discrete signal frequency within the analysis interval.

2.5.3. Time–Frequency Domain Characteristic Analysis of Vibration Signals

Through Fourier transform, the original discrete signal in the time domain can be decomposed into a series of sine signals at different frequencies, which is simpler than the original signal. However, the time domain signal after Fourier transform is difficult to reflect the relationship between frequency and time. Therefore, for the self-propelled straw pickup baler with more complex operating conditions, it is necessary to comprehensively consider the relationship between the frequency and time of the vibration signal to obtain the variation pattern of the amplitude of different frequency components over time. Thus, this paper employed time–frequency domain analysis for further investigation.

The initial time–frequency domain analysis method was the Short-Time Fourier Transform (STFT), the basic principle of which involves applying a window function to the Fourier transform process of the original signal. By moving the window function $h(t)$ along the time axis, the original signal is analyzed in segments to obtain several groups of equal-length local "spectra". These segments are then connected to derive the frequency and amplitude variation characteristics of the original signal over time. Its defining expression is:

$$STFT_f(t, f) = \int_{-\infty}^{\infty} x(t) h(\pi - t) e^{-j2\pi f \tau} d\tau \tag{19}$$

In the formula, $h(\pi - t)$ is the analysis window function centered at time τ, and $STFT_f(t, f)$ is the Short-Time Fourier Transform function concerning frequency and time. For the $STFT$ calculation formula of discrete signals, it can be expressed as:

$$STFT_f(n, k) = \sum_{m=-\infty}^{\infty} f(m) g(n - m) e^{-j\frac{2\pi k}{N}m} R_N(k) \tag{20}$$

In the formula, $R_N(K) = \begin{cases} 1, \ k = 0, 1, 2 \ldots . N - 1 \\ 0, \ other \end{cases}$, N is the number of sampling points within the window, and n is the midpoint within the window.

Considering that the vibration signal frequency of the self-propelled straw pickup baler is relatively stable, this paper selected the Short-Time Fourier Transform method for time-frequency analysis to obtain the variation characteristics of the frequency and amplitude of the vibration signal over time.

3. Results and Discussion

3.1. Analysis of Vibration Signal Intensity in Time Domain Distribution

The vibration signals obtained from the experiments were organized and calculated for the root mean square (RMS) values of acceleration in three directions under different operating conditions, as well as the peak-to-peak values of displacement obtained from the original signal through double integration. The calculation formula for the RMS value of

the acceleration vibration signal is shown in Equation (21), and the statistical results are presented in Figure 12.

$$a_{rms} = \sqrt{\frac{1}{N}\sum_{i=1}^{N} a_i^2} = \sqrt{\frac{a_1^2 + a_2^2 + \ldots + a_N^2}{N}} \quad (21)$$

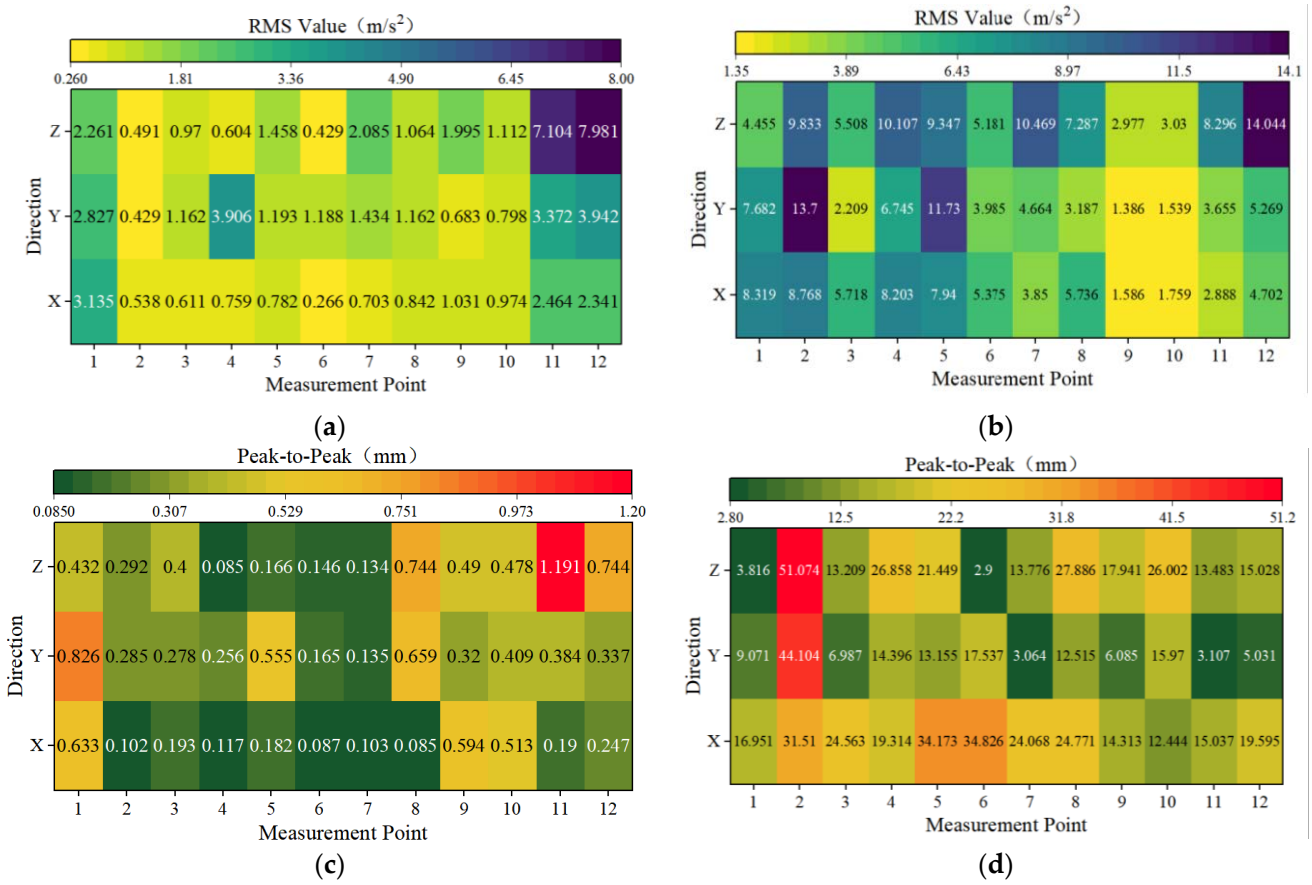

Figure 12. The heat map of vibration intensity in time domain under different operating conditions of the self-propelled straw pickup baler. (**a**) RMS value of operating condition 1; (**b**) RMS value of operating condition 2; (**c**) peak-to-peak value of operating condition 1; (**d**) peak-to-peak value of operating condition 2.

In the formula, α_i is the root mean square (RMS) value of acceleration for the i frequency band; a_{rms} is the RMS value of acceleration in a single direction, m/s^2; and N is the total number of frequency bands.

To facilitate data analysis, the data from measurement points with significant vibration at key locations are highlighted in bold. From the calculated results in Figure 12, it can be observed that under test condition 1, which involves stationary idling excitation in an indoor setting (with only the engine idling throttle in operation), the diesel engine is the sole excitation source for the entire machine. The vibration intensity in all three directions is relatively high, with the RMS values exceeding 2 m/s^2. For the other excitation source locations, the RMS values of the signals, except for the Y direction at measurement point 4, did not exceed 2 m/s^2. This is primarily because the measurement point for the rear grass rolling drum is located on the upper side of the mounting plate at the end of the drive shaft, which has two different-sized sprockets mounted coaxially to transmit power forward and backward. The reason for the higher vibration intensity at this location is that thin plate vibrations predominantly occur in a direction perpendicular to the plate surface. Additionally, the vertical direction RMS values at measurement points 7 and 9 are also close

to the RMS values in the same direction as the engine, mainly because these two points are response points on the left and right sides of the front of the frame, with the engine directly mounted in the middle of the frame. It is also noted that the Z direction vibration signal RMS values at the two response points (11 and 12) in the cab exceed 7 m/s^2, which is significantly higher than the other two directions. This is primarily due to the structural vibrations caused by the flat plate structure of the operator's platform, indicating that the vertical vibrations at the driver's position are severe, leading to poor comfort, which is consistent with the intuitive feelings experienced in the field. The vibration responses at the other measurement points have all attenuated due to the continuous weakening of the vibrations generated by the engine during transmission.

In test condition 2, which is the stationary no-load condition in an indoor setting (with operational components), both the engine and the working components are active. At this point, the effective values of the vibration acceleration signals in all three directions at each measurement point on the machine body significantly increase, leading to noticeable vibrations. It is likely that there is vibration coupling and resonance in different directions between the excitation sources. By examining the data in Figure 12, it is evident that the root mean square values of the vibration acceleration in the X and Z directions at the excitation source measurement points are relatively large. Additionally, the peak-to-peak displacement values obtained from the second integration of the acceleration signals are also largest in the X and Z directions. Meanwhile, the maximum effective and peak-to-peak values of the vibration signals at the six response measurement points on the machine body appear in the vertical direction. This indicates that the significant vibration of the machine body occurs in the longitudinal and vertical directions, which aligns with the observed vibration behavior of the entire machine in the factory setting.

To better distinguish the response characteristics of the frame with and without operational component excitation, an optimized RMS envelope spectrum method was employed to reduce the impact of sudden abnormal interference points in the vibration signal data. This allowed for a more reasonable assessment of the frame's vibration intensity. The algorithm's window size was set to 150 sample points. At this setting, the envelope signal effectively reflects the stability of the original vibration signal's intensity in three directions and better analyzes the maximum vibration value and primary vibration direction of the frame. Therefore, measurement point 7 at the front left of the frame was chosen as the representative point for frame response. The sensor's attachment location is shown in Figure 13a, where Figure 13b,c correspond to the acceleration vibration signals in three directions collected at this point under conditions 1 and 2, respectively.

From the peak level comparison of the signals under the two conditions, it can be observed that the main energy concentration area of the 7-X direction vibration acceleration increases from the order of 0.5 m/s^2 to 5 m/s^2, with the acceleration impact peak reaching 18 m/s^2 under condition 2. It is also noted that the positions of the peak points exhibit periodic changes rather than random phenomena. The average value calculated from the RMS envelope spectrum curve shows that the envelope RMS value in this direction increases from 0.74 m/s^2 to 3.83 m/s^2. In the 7-Y direction, the main peak of the impact signal under condition 2 is between 10 m/s^2 and 15 m/s^2, with an envelope effective average value of 4.59 m/s^2. Additionally, under condition 1, a phenomenon is observed where the peak value below the zero axis is significantly greater than that above, indicating that there may be an unbalanced impact force on the frame during the engine idle state. The acceleration data in the 7-Z direction shows the most dramatic changes, with local signal peaks increasing from between 5 m m/s^2 and 8 m/s^2 to between 30 m/s^2 and 40 m/s^2. The average value obtained through the RMS envelope effective value algorithm increases from 2.12 m/s^2 to 10.34 m/s^2. Therefore, a comprehensive quantitative analysis of the envelope effective values indicates that the vibration impact in the 7-Z direction is the most severe, followed by the 7-X direction.

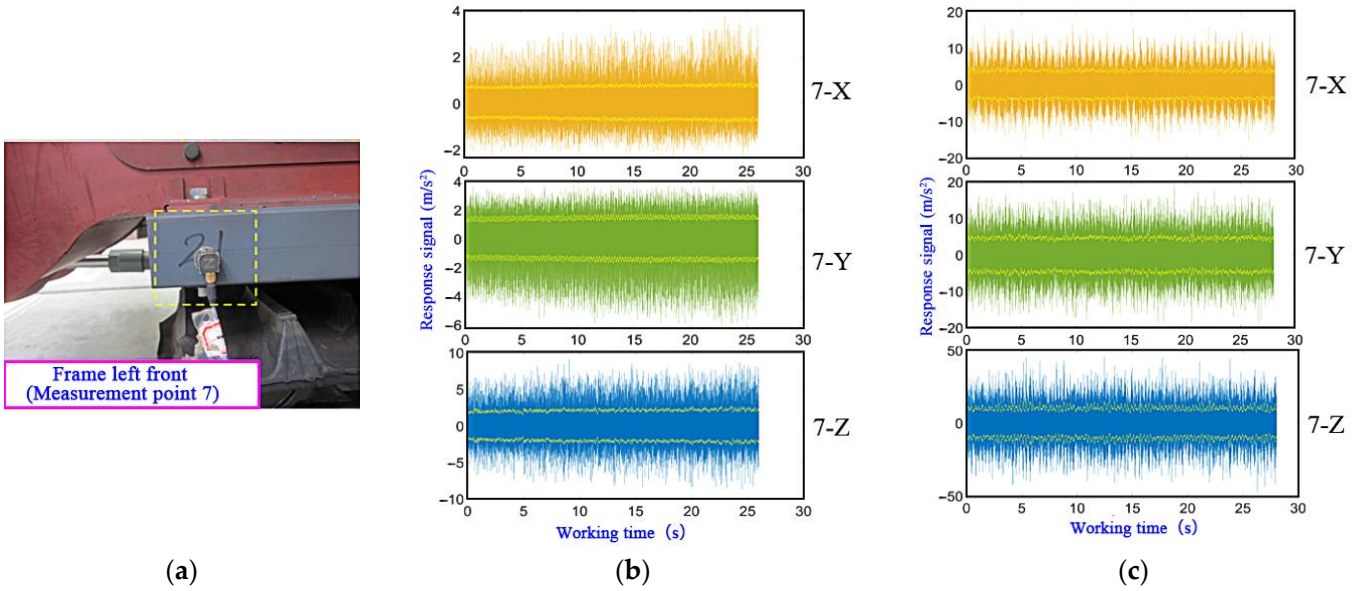

Figure 13. Comparison of sensor layout and RMS envelope spectrum signal. (**a**) Sensor layout diagram for measurement point 7; (**b**) measurement point 7 (condition 1); (**c**) measurement point 7 (condition 2).

Furthermore, by observing the statistical data in Figure 12 under condition 2, it can be found that the vibration signal effective value in the Y direction at measurement point 2, located at the front end of the entire machine's picker, is significantly greater than in the other two directions, with its time domain response shown in Figure 14a. Additionally, the peak-to-peak values of displacement in all three directions are greater than those at other measurement points. This may be due to the side measurement points being arranged as welded thin plates, which could lead to local resonance. There may also be significant transverse vibration intensity due to reciprocating forces and the excitation force interference from chain transmission, necessitating further analysis in the subsequent frequency domain and time–frequency domain analyses.

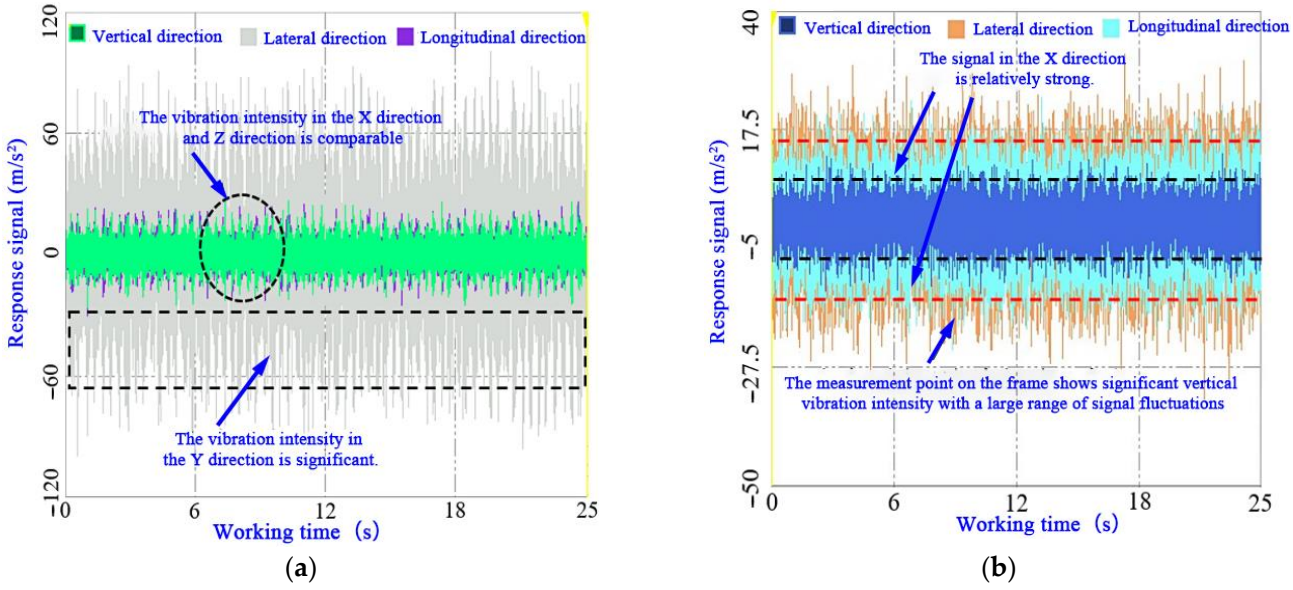

Figure 14. Time domain response of acceleration signals. (**a**) Measurement point 2; (**b**) measurement point 8.

The time domain response of measurement point 8 at the left rear end of the chassis frame is shown in Figure 14b. The signal in the Z direction is significantly greater than in the other two directions, and the signal exhibits a large range of continuous fluctuations. The effective value increases from 1.995 m/s^2 to 7.287 m/s^2. Combining this with the peak-to-peak displacement changes of the vibration signals in the X and Z directions, it can be concluded that after the working components start operating, the longitudinal vibration of the chassis becomes evident, with significant longitudinal amplitudes at the front and rear ends of the frame. In contrast, the effective value changes of the vibration response measurement points 9 and 10 located on the feed box show little increase, indicating that the vibration from the excitation source experiences significant attenuation when transmitted to the feed box, which is related to the layout of the key moving components of the machine.

Therefore, to study the longitudinal amplitude response of the frame under normal walking conditions, this experiment conducted vibration tests under two different conditions: engine idle throttle operation and operation of the working components, while the machine was walking unloaded in an outdoor area. The response measurement points were mainly arranged at the top cover position of the left half of the machine body. The measurement point numbers were arranged from 1 to 8 in the direction of the machine's forward movement, with a distance of 10 cm between adjacent measurement points. By performing a second integration calculation on the acceleration signals, the positive and negative vibration amplitudes in three directions for each measurement point were obtained, as shown in Figure 15.

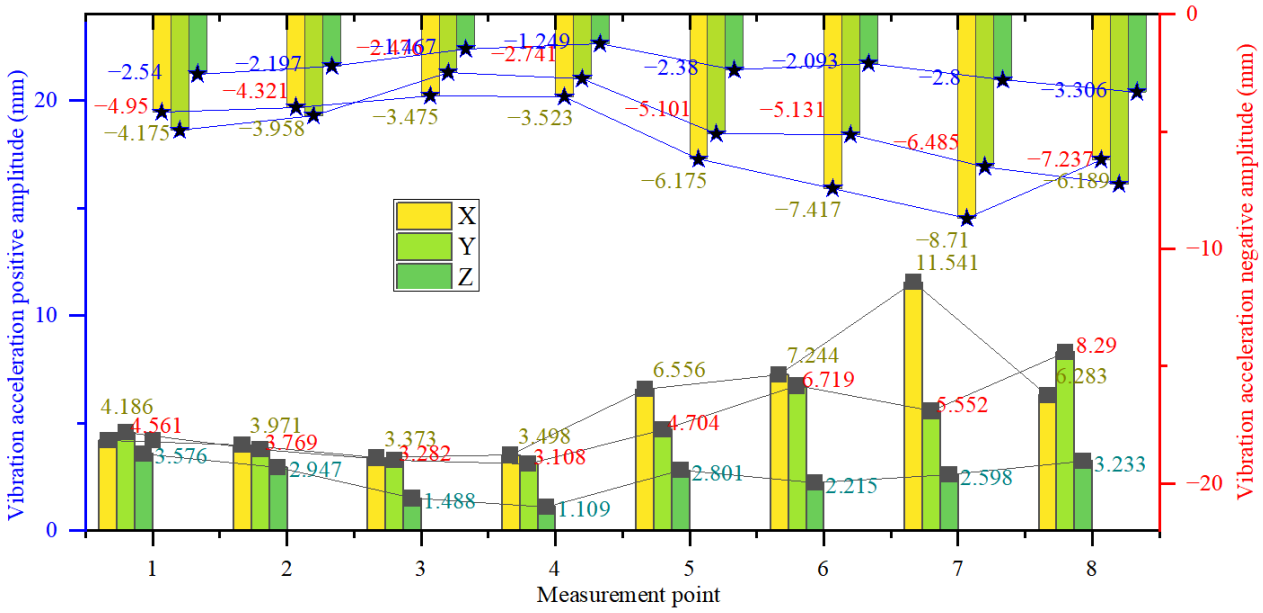

(**a**)

Figure 15. *Cont.*

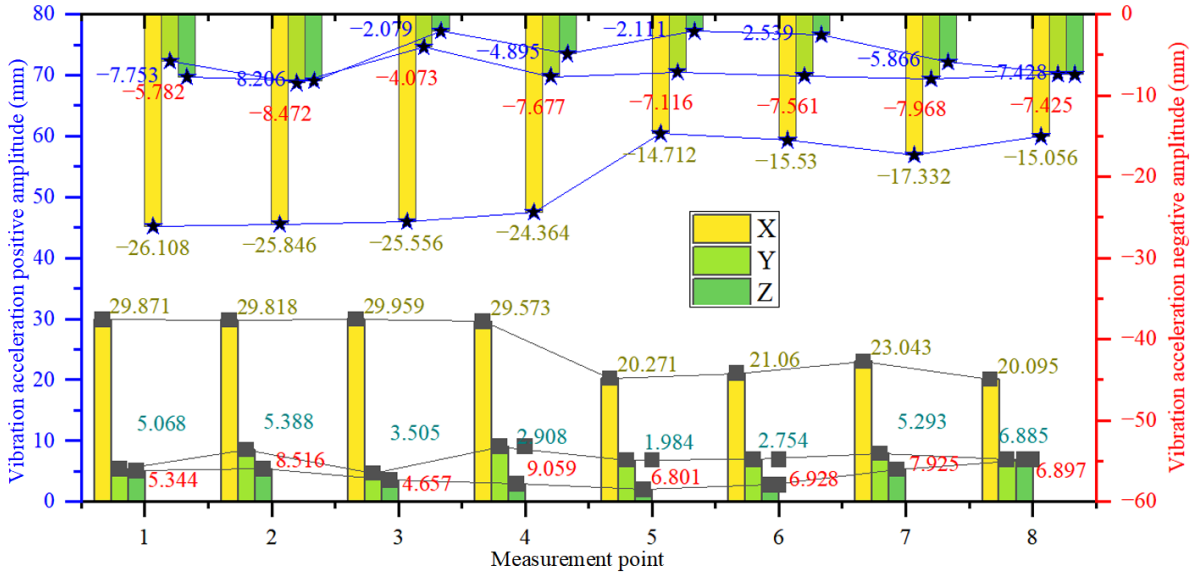

(**b**)

Figure 15. Comparison of vibration intensity in time domain under different conditions for the pickup baler in outdoor testing. (**a**) Positive and negative amplitude of vibration acceleration under test condition 3; (**b**) positive and negative amplitude of vibration acceleration under test condition 4.

It can be observed that when the machine transitions from condition 3 to condition 4, all eight measurement points exhibit the largest amplitude change in the X direction. The positive vibration amplitude of the frontmost measurement point 1 increases from 4.186 mm to 29.871 mm, indicating that the longitudinal vibration of the machine body becomes very evident after the key components of the machine start operating. Under condition 3, the amplitudes in the X and Z directions at each measurement point show a trend of gradually decreasing from points 1 to 4 and then gradually increasing to point 8. After the working components start running, the amplitudes at each measurement point increase significantly, showing a trend of gradually decreasing from points 1 to 5 and then gradually increasing to point 7 in the X and Z directions. This indicates that the position between measurement points 4 and 5 is continuously approaching the longitudinal center of gravity of the entire machine, and the longitudinal vibration amplitude at this position also increases from 1.1 mm to 2.9 mm, which is consistent with the trend of the multi-degree-of-freedom dynamic model simulation results mentioned earlier, confirming the validity of the mechanical model.

3.2. The Amplitude and Frequency Comparison Under Frequency Domain Signal Transformation

The pickup baler was equipped with a four-cylinder diesel engine with a rated operating speed of 2400 r/min. The excitation generated by the engine was mainly due to the periodic excitation force produced by combustion and the unbalanced inertial force of the connecting rod mechanism. The calculation formula for the combustion excitation frequency of the four-cylinder diesel engine is:

$$f_0 = \frac{n_0 i}{60c} \tag{22}$$

In the formula, f_0 is the engine combustion excitation frequency, Hz; n_0 is the engine speed, r/min; i is the number of cylinders in the diesel engine; and c is the number of strokes of the engine. The rotational inertial force excitation caused by the engine's connecting rod mechanism can be calculated using Formula (23):

$$f_1 = \frac{Qn_0}{60} \tag{23}$$

In the formula, f_1 is the inertial force excitation frequency, Hz; Q is the engine proportionality coefficient, which is 2 in this case. Therefore, the theoretical rotational excitation frequency of the diesel engine can be calculated to be 40 Hz, and the excitation frequency caused by combustion and inertial forces is 80 Hz, which corresponds to the second-order ignition working frequency at the rated speed of the engine. The frequency spectrum characteristics of the engine under this operating condition are obtained by applying FFT transformation to the vibration time domain signal, as shown in Figure 16.

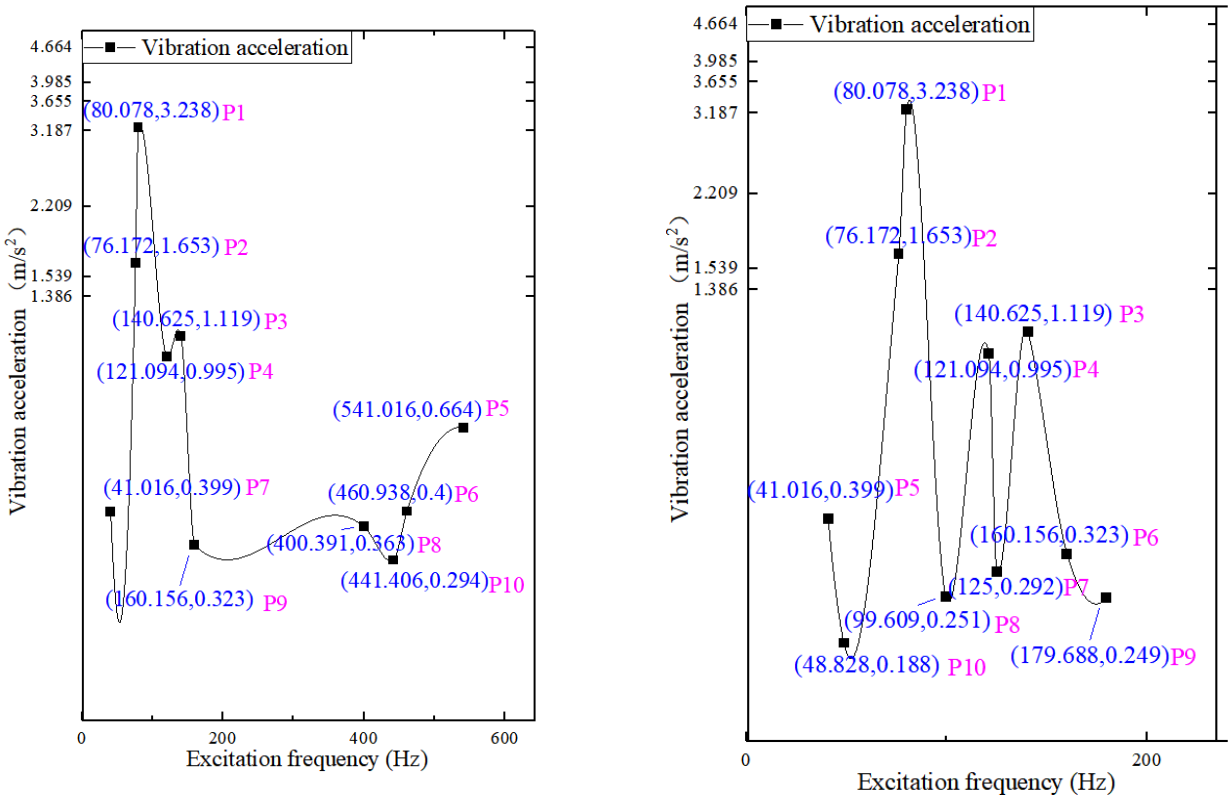

Figure 16. Idle throttle engine frequency spectrum (X direction). (**a**) First ten peak frequencies; (**b**) low-frequency band enlarged display.

From the figure, it can be seen that the peak value of the vibration acceleration at this measurement point in the X direction is the largest at a frequency of 80.078 Hz, which is also the main frequency of the engine vibration under idle throttle conditions. This test value is close to the calculated second-order ignition working frequency. Additionally, a harmonic component at 160.156 Hz is also observed, confirming the accuracy of the experiment. Furthermore, the time domain signal with relatively small fluctuations under condition 1 (idle throttle operation of the engine only) in the indoor testing site was selected. After applying the fast Fourier transform, the first four peak values of the acceleration signals and their corresponding vibration frequencies are shown in Figure 17.

It can be seen that the main vibration frequencies at various measurement points of key components and the frame response points in three directions frequently occur at frequencies such as 39.063 Hz, 80.078 Hz, and 158.203 Hz. These correspond to the rotational frequency and various harmonic frequencies of the engine under idle conditions. Additionally, the peak vibration signal at the engine mount position is largest in the X direction, followed by the Z direction and Y direction. This is primarily due to the installation method of the engine, which causes the longitudinal excitation force to decompose into the other two directions.

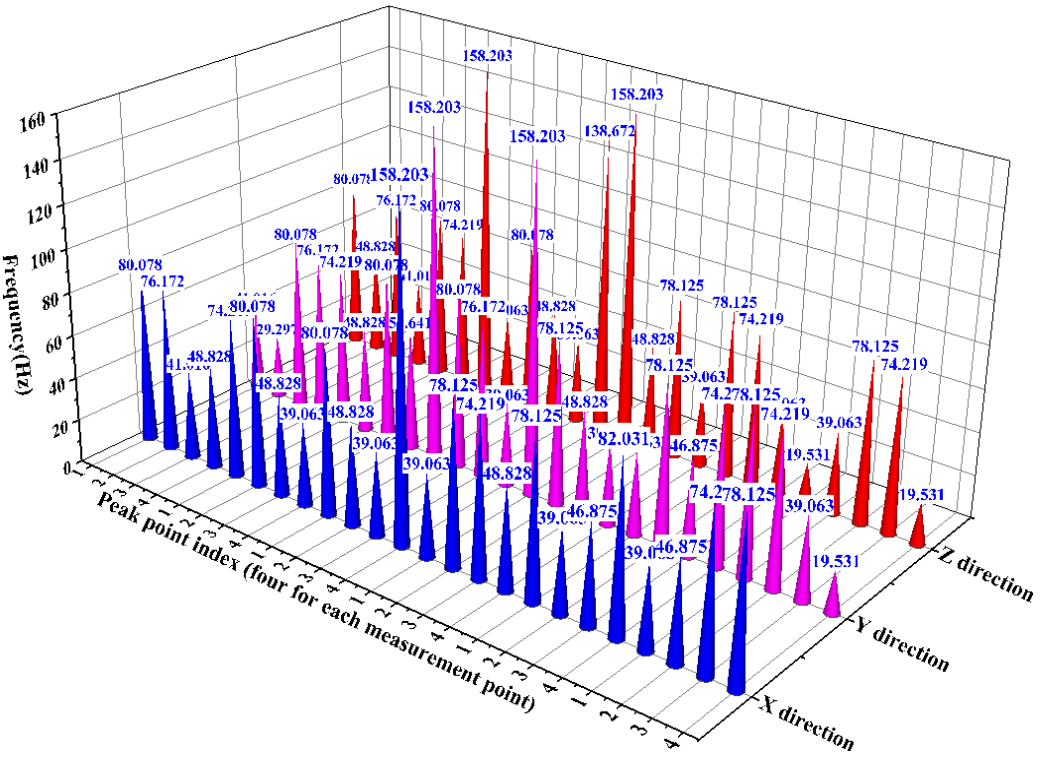

Figure 17. The frequencies of each measurement 1~6 point under condition 1.

Furthermore, measurement points 7 to 10 are frame response points, and their signals exhibit relatively small amplitudes compared to the other key moving components, as shown in Figure 18. In contrast, measurement points 11 and 12, located at the driver's cabin, show larger amplitude peaks in all three directions. This indicates that under idle conditions, the engine, as the sole excitation source of the body, has a significant impact on the vibration intensity at the driver's cabin position.

When the entire machine is in a stationary, no-load condition (operating components) in indoor condition 2, the peak vibration signals at different measurement point locations show a significant increase. By analyzing the time domain signals, the direction of maximum vibration intensity for each measurement point can be determined. Therefore, a Short-Time Fourier Transform is applied to obtain the frequency responses in the Z direction for measurement points 1-X, 2-Y, 3-X, 4-Z, 5-Z, 6-X, and 7-12. Specifically, measurement points 4-Z, 7-Z, and 6-X exhibit sidebands centered around high-frequency signals, while measurement points 3-X, 5-Z, 8-Z, and 12-Z show sidebands primarily composed of mid-frequency components. Additionally, other measurement points, aside from effective low-frequency signals, also contain a significant amount of interference signals. The generation of these random interference signals is mainly due to the resonance and friction caused by the movable connection between the working components and the frame, which manifests in the frequency spectrum as wideband frequency signals rather than a few sharp peak points.

Therefore, based on the time domain characteristics of the measurement point signals and the distribution in the frequency spectrum, measurement points 1-X, 6-X, 2-Y, 7-Z, 8-Z, and 12-Z were analyzed by removing interference frequencies and retaining only the effective low-frequency signals in the range of 0 to 200 Hz. The processed frequency spectrum distribution is shown in Figure 19. The frequency f represents the excitation frequency of the diesel engine, the frequency f_1 represents the excitation frequency of the compression mechanism, the frequency f_2 represents the excitation frequency of the intermediate shaft, and the frequency f_3 represents some excitation frequencies of the screw conveyor.

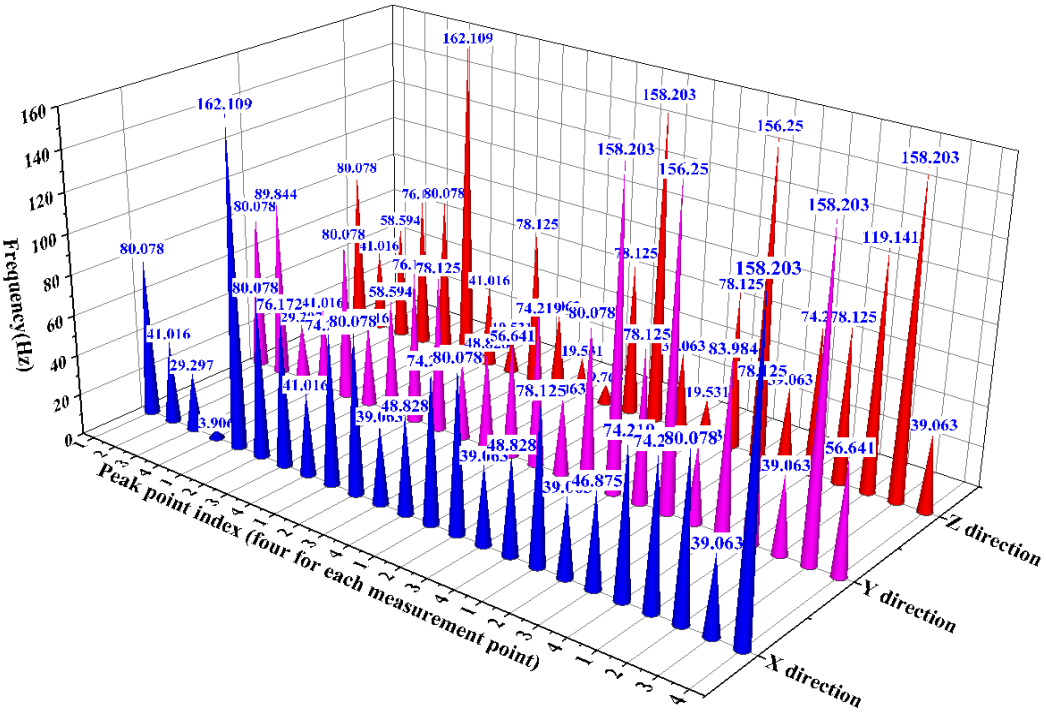

Figure 18. The frequencies of each measurement 7~12 point under condition 1.

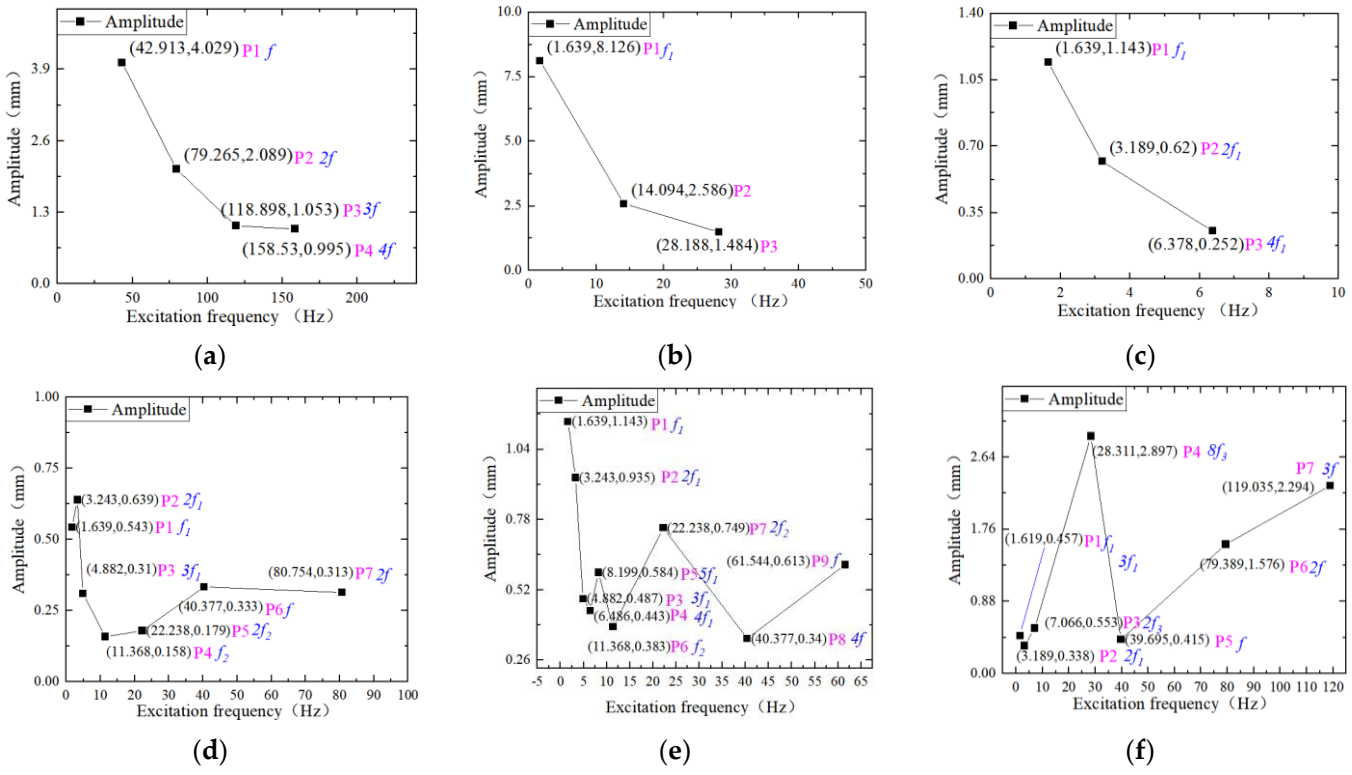

Figure 19. Low-frequency component frequency spectrum. (**a**) Measurement point 1-X; (**b**) measurement point 2-Y; (**c**) measurement point 6-X; (**d**) measurement point 7-Z; (**e**) measurement point 8-Z; (**f**) measurement point 12-Z.

It can be observed that the vibration frequency at measurement point 1-X, located at the engine's frame connection, mainly includes its fundamental frequency and various harmonic frequencies. Figure 19c shows the low-frequency component frequency spectrum

in the forward and backward directions of the compression mechanism. It can be found that the main frequency components at this location are relatively simple, primarily including the rotational excitation frequency of the compression mechanism's drive shaft at 1.639 Hz, its second harmonic at 3.189 Hz, and its fourth harmonic at 6.378 Hz. This is mainly due to the periodic impact force generated by the reciprocating motion of the compression slider. Furthermore, this working frequency and its harmonics repeatedly appear in the first few major peak vibration frequencies of other key moving component measurement points and the structural response points of the machine body, indicating that the low-frequency vibrations during the operation of the compression mechanism affect the response of the entire machine structure.

Additionally, the corresponding vibration frequency at measurement point 2, located at the picker drive shaft bearing seat, has amplitude peaks exceeding 3.0 m/s^2 in the X, Y, and Z directions, with amplitudes being two to three times that of the second peak. Notably, under the main vibration frequency of the compression mechanism at 1.639 Hz, the lateral vibration signal peak at this measurement point reaches 8.126 m/s^2. This indicates that the picker drive shaft position is likely experiencing local resonance due to the periodic excitation force from the compression mechanism at the fundamental frequency of 1.639 Hz and its second harmonic at 3.189 Hz. It can also be concluded that the vibration generated at this position is a major reason for the significant amplitude in the lateral direction of the machine body.

Based on the data from the machine body response measurement points 7-Z, 8-Z, and 12-Z, it can be observed that the vibration peak in the Z direction is quite pronounced, with the maximum amplitude occurring around a frequency of 1.6 Hz, followed by the forward and backward directions. In addition to the working frequency of the compression mechanism and its harmonics, there are also frequencies close to that of measurement point 1-X, as well as some excitation frequencies of the intermediate shaft. This indicates that the large longitudinal vibration amplitude of the machine body is primarily due to the periodic excitation force generated during the operation of the compression mechanism. It also suggests that the reciprocating motion excitation force of the compression mechanism is an important component of the overall machine vibration, serving as the second source of vibration affecting the frame response, following the engine. Consequently, the center of gravity of the machine body experiences periodic amplitude changes.

3.3. Analysis of Time–Frequency Domain Characteristics of Signals Under Multiple Operating Conditions

During the experimental testing process, the vibration signals collected by the sensors often contain random signals and high-frequency interference signals, which can affect the processing of the time–frequency domain characteristics of the signals. To analyze the energy distribution of the vibration signals over the entire testing period, the Signal Analyzer tool in MATLAB (2021b) was used for processing. By applying a low-pass filter to the original signals, the frequency was limited to within 200 Hz to ensure that the analyzed signals primarily consisted of effective low-frequency components.

Combining this with the previous frequency domain analysis, it is known that the two excitation frequencies at this response measurement point 8 mainly correspond to the harmonic frequencies generated by the engine's combustion excitation and the continuous low-frequency vibrations of the compression mechanism, as shown in Figure 20. Therefore, when the compression mechanism begins to operate, the periodic reciprocating compression motion of the crank-slider mechanism generates continuous impacts on the frame, leading to periodic changes in the vibration amplitude of the chassis frame. The waterfall plots of the amplitude spectrum for the other measurement points are shown in Figure 21.

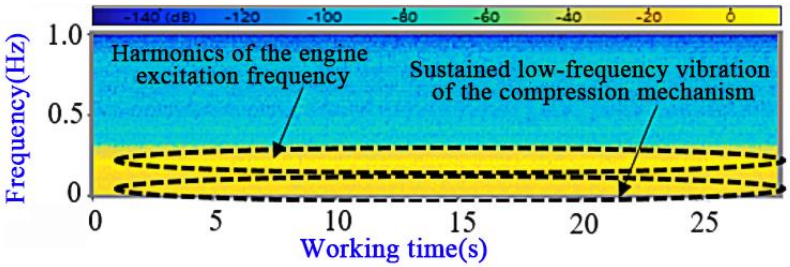

Figure 20. Comparison diagram of signal filtering before and after filtering at measuring point 8 on the left rear of the chassis frame.

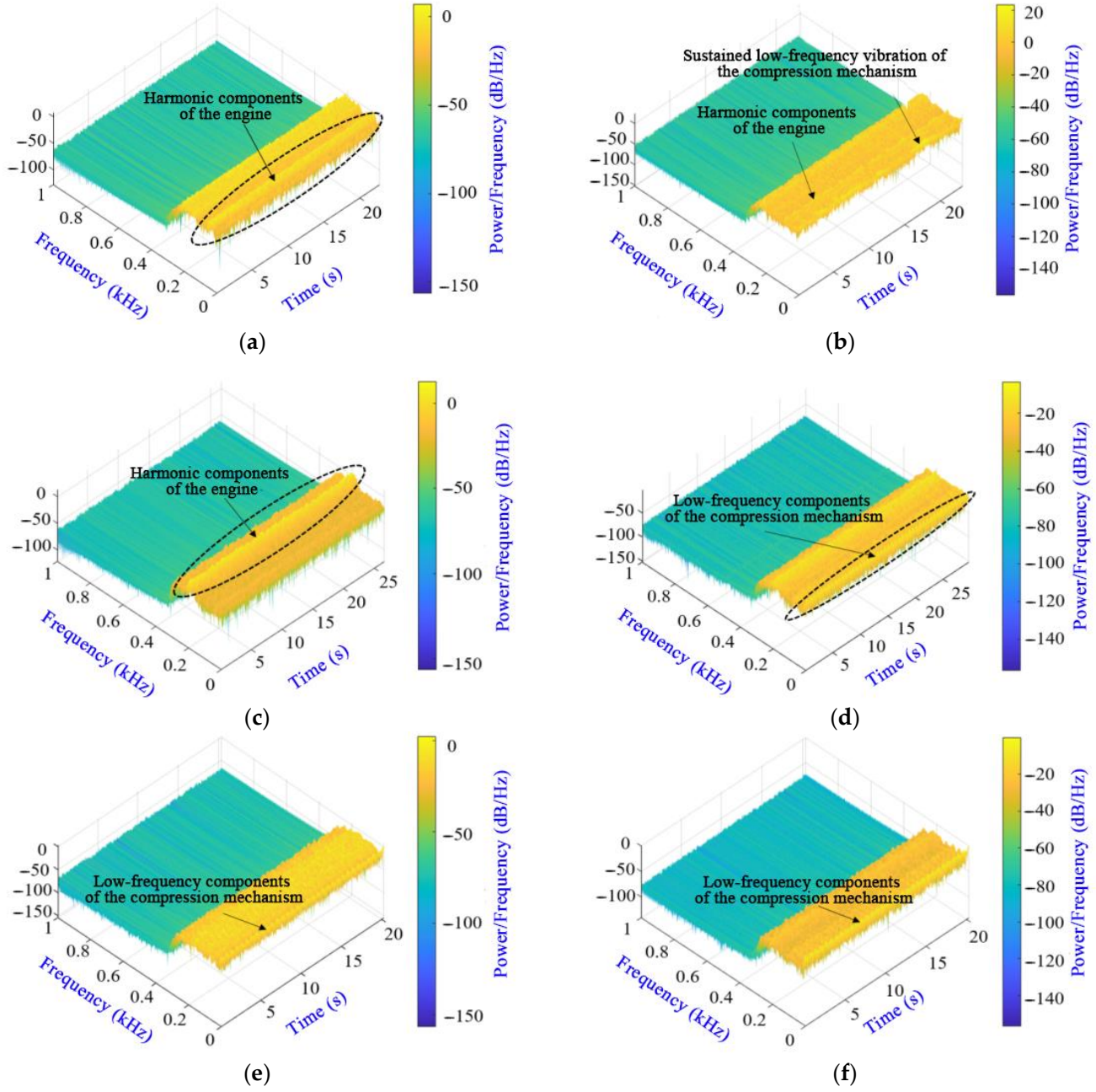

Figure 21. Amplitude spectrum waterfall plots of each measurement point. (**a**) Time–frequency map of 1-X point; (**b**) time–frequency map of 2-Y point; (**c**) time–frequency map of 3-X point; (**d**) time–frequency map of 4-Z point; (**e**) time–frequency map of 5-Z point; (**f**) time–frequency map of 6-X point.

When the working components begin to move, the harmonic components of the excitation frequency at the engine's rated speed have a significant impact at the positions of its supports, the picker drive shaft support, and the front grass rolling drum drive shaft support. It is clear that the waterfall plot exhibits distinct frequency peaks, and the signals consistently and stably influence the testing period. Multiple measurement points under operating condition 2 show significant low-frequency components that tend to stabilize, indicating that the periodic motion of the compression mechanism has a substantial and continuous impact on the low-frequency components at each measurement point location.

4. Conclusions

(1) The structure of the self-propelled straw pickup baler is complex, with multiple excitation sources. Each key working component has different installation methods and motion forms, causing the vibration state of the machine body to change continuously. This paper conducts a mechanical analysis of the various structures of the self-propelled straw pickup baler and establishes balance equations to analyze the vibration sources and main working devices of the machine. Furthermore, it studies the theoretical characteristics of the vibration excitation forces of each device to analyze the effects of different devices and structures under internal and external excitation. This paper aims to understand the action of excitation forces from different devices, laying a theoretical foundation for the experimental investigation of excitation coupling in each device.

(2) To explore the impact of different operating states of the self-propelled picking and baling machine on the vibration coupling characteristics of each working device, experiments were conducted to collect excitation signals from multiple devices. The results showed that the effective value of the Z-direction vibration signal on the left front of the chassis frame exceeded 7 m/s^2, while the right front increased from 1.995 m/s^2 to 7.287 m/s^2, indicating intense vibrations. Additionally, the effective values at measurement points 11 and 12 in the cab also exceeded 7 m/s^2, indicating significant longitudinal and vertical vibrations. This aligns with the device balance calculation model. The analysis revealed that the excitation from each device significantly affects other structures, particularly in the Z direction. This provides a foundation for optimizing the connection structure of the devices to enhance excitation transmission in the self-propelled picking and baling machine.

(3) To investigate the coupling excitation effects of each device under different operating states, the Signal Analyzer module in MATLAB was used to analyze the signal characteristics of each measurement point. The filtered signals showed harmonic frequencies from combustion excitation and continuous low-frequency vibrations from the compression mechanism. The periodic motion of the compression mechanism causes continuous impacts on the frame, leading to periodic changes in chassis vibration amplitude. The analysis indicated that the compression mechanism's motion significantly affects low-frequency components at each measurement point, suggesting that optimizing its vibration reduction is key to minimizing overall machine vibration.

Author Contributions: B.W. proposed the overall concept of the article, participated in data management, used analytical software for data visualization, and wrote the initial draft of the article. K.Q. and H.W. reviewed and revised the article. Additionally, during the experiments, B.W., K.Q., H.W., and others designed and conducted the experiments, while mentors Z.T., Y.L., and M.S. provided guidance for the experiments. The materials, reagents, analytical tools, and funding for this article were all provided by mentors Z.T., Y.L., and M.S. All authors have read and agreed to the published version of the manuscript.

Funding: This research work was supported by the Nantong Science and Technology Project Social Livelihood Science and Technology Plan (MS2023016), Key Laboratory of Modern Agricultural Equipment and Technology (Jiangsu University), and Ministry of Education (MAET202326), A Project Funded by the Priority Academic Program Development of Jiangsu Higher Education Institutions (No. PAPD-2023-87).

Data Availability Statement: The data used to support the findings of this study are available from the corresponding author upon request.

Conflicts of Interest: The authors declared that there are no conflicts of interest.

References

1. Zhang, S.; Dai, F.; Zhao, W.; Tian, B.; Chen, B. Design and test of matching straw baling device for highland barley combine harvester. *Acta Agric. Zhejiangensis* **2020**, *32*, 1289–1301.
2. Li, Y.; Xu, L.Z.; Lv, L.Y.; Shi, Y.; Yu, X. Study on Modeling Method of a Multi-Parameter Control System for Threshing and Cleaning Devices in the Grain Combine Harvester. *Agriculture* **2022**, *12*, 1483. [CrossRef]
3. Liang, Z.W.; Wada, M.E. Development of cleaning systems for combine harvesters: A review. *Biosyst. Eng.* **2023**, *236*, 79–102. [CrossRef]
4. Fan, G.; Liu, C.; Lou, Y.; Wu, J.; Liu, H.; Li, S.; He, D. Research on dynamic characteristics of complete dynamic model of vibrating screen based on spatial six degrees of freedom. *J. China Univ. Min. Technol.* **2024**, *53*, 176–185.
5. Tang, J.; Xiong, X.; Wu, B.; Cao, R. Coupling Vibration Analysis Between Flip-Flow Screen Panels and Moist Fine Coal Material Containing Agglomerates. *J. Vib. Meas. Diagn.* **2022**, *42*, 1099–1107.
6. Zhang, T.; Li, Y.M.; Xu, L.Z.; Liu, Y.B.; Ji, K.Z.; Jiang, S. Experimental Study on Fluidization Behaviors of Wet Rice Threshed Materials with Hot Airflow. *Agriculture* **2022**, *12*, 601. [CrossRef]
7. Wang, F.Z.; Liu, Y.B.; Li, Y.M.; Ji, K.Z. Research and Experiment on Variable-Diameter Threshing Drum with Movable Radial Plates for Combine Harvester. *Agriculture* **2023**, *13*, 1487. [CrossRef]
8. Chen, L.; Tao, L. Modeling and Characteristic Analysis of Torsional Vibration of HEV Driveline Excited by Multi-source Harmonics. *Noise Vib. Control.* **2023**, *43*, 1.
9. Xiao, W.; Zhu, Y.; Lu, C.; Liu, Z.E. Research on structural load simulation method of road noise. *Tech. Acoust.* **2023**, *42*, 495–502.
10. Guo, X.; Yang, Y.; Wang, C.; Ling, L.; Wang, K.; Zhai, W. Influence of Wheel/Rail Dynamic Interaction Induced by Polygonal Wheels Under Braking Condition. *J. Mech. Eng.* **2023**, *59*, 196–203.
11. Liu, W.; Zong, W.; Ma, L.; Lian, G.; Li, M. Influencing factors of falling seeds loss at header and seed hull damage of edible sunflower. *Trans. Chin. Soc. Agric. Eng.* **2023**, *39*, 54–62.
12. Ma, Z.; Wu, Z.P.; Li, Y.F.; Song, Z.Q.; Yu, J.; Li, Y.M.; Xu, L.Z. Study of the grain particle-conveying performance of a bionic non-smooth-structure screw conveyor. *Biosyst. Eng.* **2024**, *238*, 94–104. [CrossRef]
13. Liu, Y.B.; Li, Y.M.; Zhang, T.; Huang, M.S. Effect of concentric and non-concentric threshing gaps on damage of rice straw during threshing for combine harvester. *Biosyst. Eng.* **2022**, *219*, 1–10. [CrossRef]
14. Li, Y.M.; Liu, Y.B.; Ji, K.Z.; Zhu, R.H. A Fault Diagnosis Method for a Differential Inverse Gearbox of a Crawler Combine Harvester Based on Order Analysis. *Agriculture* **2022**, *12*, 1300. [CrossRef]
15. Sun, X.; Lu, Z.; Chen, Y. Fatigue Life Analysis of Hydro-mechanical Continuously Variable Transmission Box of Heavy Tractor. *Mech. Sci. Technol. Aerosp. Eng.* **2022**, *41*, 1844–1851.
16. Zhang, Z.; Yin, Q.; Chen, Z.; Pu, H.; Li, Y.; Zhang, J. Topology Optimization of Car Body Damping Materials Based on Transfer Path Analysis. *Noise Vib. Control.* **2022**, *42*, 167–172.
17. Zong, Y.; Zhang, Q.; Yang, Y.; Jiang, C.; Luo, Z. Numerical Simulation Research of Vehicle Windshield Noise Based on LBM-FE-SEA Method. *Noise Vib. Control.* **2022**, *42*, 184.
18. Lu, C.; Li, Y.; Liu, Z.; Li, Q.; Luo, T.; Xu, Y. Vehicle structural road noise transmission path under wheel excitation. *J. Vib. Shock.* **2021**, *40*, 42.
19. Zhu, Z.; Zhu, J.; Liu, Q.; Gong, X.; Cheng, S. Analysis and Control of Structural Noise in Excavator Cabs. *Noise Vib. Control.* **2020**, *40*, 131–136.
20. Jiang, M.; Xiang, Y. Fault Diagnosis for Marine Diesel Engines Base on AE-ANFIS. *Noise Vib. Control.* **2023**, *43*, 188.
21. Li, H.B.; Chen, L.W.; Zhang, Z.Y. A Study on the Utilization Rate and Influencing Factors of Small Agricultural Machinery: Evidence from 10 Hilly and Mountainous Provinces in China. *Agriculture* **2023**, *13*, 51. [CrossRef]
22. Li, Q.; Song, Y.; Yao, C.; Li, W.; Yue, Y. Intelligent Design and Optimization System for Cleaning Device of Rice and Wheat Combine Harvester. *Trans. Chin. Soc. Agric. Mach.* **2021**, *52*, 92–101.
23. Badretdinov, I.; Mudarisov, S.; Lukmanov, R.; Permyakov, V.; Ibragimov, R.; Nasyrov, R. Mathematical modeling and research of the work of the grain combine harvester cleaning system. *Comput. Electron. Agric.* **2019**, *165*, 104966. [CrossRef]
24. Ma, Z.; Zhang, Z.L.; Zhang, Z.H.; Song, Z.Q.; Liu, Y.B.; Li, Y.M.; Xu, L.Z. Durable Testing and Analysis of a Cleaning Sieve Based on Vibration and Strain Signals. *Agriculture* **2023**, *13*, 2232. [CrossRef]

25. Hu, J.P.; Xu, L.Z.; Yu, Y.; Lu, J.; Han, D.L.; Chai, X.Y.; Wu, Q.; Zhu, L.J. Design and Experiment of Bionic Straw-Cutting Blades Based on Locusta Migratoria Manilensis. *Agriculture* **2023**, *13*, 2231. [CrossRef]
26. Liu, C.; Dang, Z.; Liu, Y.; Liu, R.; Xu, P.; Wang, L.; Ma, H. Study on temperature and wear behavior of disc cutter in cutting coal rock. *J. China Coal Soc.* **2023**, *48*, 3589–3603.
27. Li, Z.; Chi, M.; Yang, C.; Zhou, Y.; Tang, J.; Luo, Y. On inverse identification method of bearing load based on railway vehicle acceleration. *J. Railw. Sci. Eng.* **2023**, *20*, 1983–1993.
28. Chen, Z.; Liu, Y.; Zhou, Z.; Ning, J. Summary of dynamics research on traction power transmission system of rail transits. *J. Traffic Transp. Eng.* **2021**, *21*, 31–49.
29. Fang, P.J.; Cai, Y.F.; Chen, L.; Wang, H.; Li, Y.C.; Sotelo, M.A.; Li, Z.X. A high-performance neural network vehicle dynamics model for trajectory tracking control. *Proc. Inst. Mech. Eng. Part D J. Automob. Eng.* **2023**, *237*, 1695–1709. [CrossRef]
30. Xu, J.; Feng, Z.; Li, H.; Liu, X. Study on Vibration Amplitude and Force Identification of Cables of Cable-stayed Bridge Based on Dynamic Monitoring. *J. Highw. Transp. Res. Dev.* **2022**, *39*, 111–116.
31. Zhang, T.; Li, Y.M.; You, G.L. Experimental Study on the Cleaning Performance of Hot Air Flow Cleaning Device. *Agriculture* **2023**, *13*, 1828. [CrossRef]
32. Wang, X.; Wang, G.; Xiang, J.; Huang, Z.; Sui, G. Roller Bearing Fault Recognition Method Based on Cyclic Autocorrelation and Multi-Domain Kernel Limit Learning Machine. *J. Mech. Strength* **2020**, *42*, 1302–1309.
33. Luo, Z.; Fan, X.; Liu, F.; Chen, H.; Zheng, R. A method for predicting vibration fatigue life of notched specimens under multi-axial coupled random excitation. *J. Vib. Shock.* **2023**, *42*, 105–113.
34. Chen, C.; Yang, G.; Xiao, S.; Zhu, T.; Xiao, F.; Gao, T. Structural Optimization of Gearbox Cases Based on Fatigue Life Prediction. *J. Mech. Strength* **2021**, *43*, 447–452.
35. Wang, T.; Xiao, F.; Jia, H.; Yin, H. Fatigue life prediction of bogie frames under random vibration based on the multi-dimensional and multi-support pseudo excitation method. *J. Vib. Shock.* **2020**, *39*, 192–197.
36. Wang, X.; Hou, Y.; Sun, S.; Li, Q.; Ren, Z. Advances in Key Mechanical Parameters for Reliability Assessment of High-Speed Train Bearings. *Chin. J. Theor. Appl. Mech.* **2021**, *53*, 19–34.
37. Shen, Z.; Fang, J.; Tang, L.; Yang, M.; Yang, J.; Wang, Y. Vibration fatigue analysis of traction motor structure based on frequency domain structural stress method. *J. Railway Sci. Eng.* **2022**, *19*, 814–821.
38. Lei, W.; Yaru, L.; Hanying, X. Review: Recent Developments in Dynamic Load Identification for Aerospace Vehicles Considering Multi-source Uncertainties. *Trans. Nanjing Univ. Aeronaut. Astronaut.* **2021**, *38*, 271–287.
39. Zhou, P.; Xin, J.; Ding, J. Least Squares Support Vector Machine Method for Load Identification of Nonlinear Systems. *Noise Vib. Control.* **2021**, *41*, 9. [CrossRef]
40. Zhu, D.; Xue, R.; Cao, X. Vehicle random vibration analysis using a SDOF parametric excitation model. *J. Vib. Shock.* **2022**, *41*, 79–86.
41. Wu, S.; He, Z.; Yin, J.; Chen, S. Identification of annularly distributed random dynamic load between satellite and rocket in frequency domain. *J. Southeast Univ. Nat. Sci. Ed.* **2022**, *52*, 825–832.
42. Xia, P.; Yang, T.; Xu, J.; Wang, L.; Yang, Z. Reversed time sequence dynamic load identification method using time delay neural network. *Acta Aeronaut. Astronaut. Sin.* **2021**, *42*, 224452.
43. Jia, H.; Huang, H.; Qiu, Z. Random Vibration Fatigue Analysis and Optimization Design of Automobile Front Bumper. *Eng. Plast. Appl.* **2023**, *51*, 63–68.
44. Wang, Z.; Ding, Y.; Ge, B.; Yuan, Z.; Xin, Y. Review on nonlinear model updating for bridge structures. *J. Traffic Transp. Eng.* **2022**, *22*, 59–75.
45. Zhang, G.; Hu, J.; Zhao, Y.; Xiong, X.; Zhao, P.; Fang, X.; Wang, Y. Analysis and identification method of railway station building structure damage based on Bayesian theory. *Build. Sci.* **2022**, *38*, 42–48.
46. Liu, M.; Peng, Z. Structural Damage Detection Based on the Excitation Points Optimization and Energy of Signals. *J. Mech. Strength* **2021**, *43*, 554–560.
47. Zhu, J.; Lu, J.; Yang, X. Identification Method of Bearing Separation of Curved Girder Bridge Based on Statistics Indicator. *J. Vib. Meas. Diagn.* **2024**, *44*, 225–231.
48. Gao, J.; Liu, Z.; Gu, W.; Zhang, F.; Zhu, L.; Xu, J. Modal Analysis and Optimization of Grain Combine Harvester Undercarriage Frame. *Mach. Des. Res.* **2023**, *39*, 199–205.
49. Guo, J.; Liu, Y.; Wei, Y.; Zhou, J.; Shi, Y. Vibration characteristics analysis of the optimal structure of integrated straw returning and residual film recycling machine. *Trans. Chin. Soc. Agric. Eng.* **2024**, *40*, 155–163.
50. Lin, T.; Zhang, T.; Zhang, Y.; Yin, Y.; Deng, X.; Pang, Y.; Luo, S. Modal analysis and structural optimization design of small corn thresher frame. *Agric. Res. Arid. Areas* **2022**, *40*, 277–284.
51. Wu, J.; Li, W.; Fang, Z.; Tong, C.; Xu, X. Fault diagnosis method of spiral bevel gear based on physical model driven optimal WPD. *J. Electron. Meas. Instrum.* **2023**, *37*, 214–222.
52. Liu, W.; Luo, X.; Zeng, S.; Zeng, L. Performance test and analysis of the self-adaptive profiling header for ratooning rice based on fuzzy PID control. *Trans. Chin. Soc. Agric. Eng.* **2022**, *38*, 1–9.

53. Chen, S.R.; Zhou, Y.P.; Tang, Z.; Lu, S.N. (2020). Modal vibration response of rice combine harvester frame under multi-source excitation. *Biosyst. Eng.* **2020**, *194*, 177–195. [CrossRef]
54. Fan, W.; Shu, C.; Wan, X.; Liao, Y.; Liao, Q.; Yang, J. Topology optimization and test of the header frame of rapeseed windrower based on the variable density method. *J. Huazhong Agric. Univ.* **2023**, *42*, 227–236.